DOI: 10.1002/chem.200700052

Metal–Metal Electronic Coupling in *syn* and *anti* Stereoisomers of Mixed-Valent $(FeCp)_2$-, $(RhL_2)_2$-, and $(FeCp)(RhL_2)$-*as*-Indacenediide Ions

Saverio Santi,*[a] Laura Orian,[a] Christian Durante,[a] Eva Zsuzsanna Bencze,[a] Annalisa Bisello,[a] Alessandro Donoli,[a] Alberto Ceccon,*[a] Franco Benetollo,[b] and Laura Crociani[b]

Abstract: The extent of metal–metal electronic coupling was quantified for a series of *syn* and *anti* stereoisomers of $(FeCp)_2$-, $(RhL_2)_2$- and $(FeCp)(RhL_2)$-(L_2 = 1,5-cyclooctadiene (cod), L = CO) *as*-indacenediide mixed-valent ions by spectroelectrochemical and DFT studies. The effect of the *syn*/*anti* orientation of the metal units with respect to the planar aromatic ligand indicates that electron transfer occurs through the bridge rather than through space. The nature of the metal was found to be crucial: while homobimetallic diiron species are localised valence-trapped ions (Class II), the dirhodium analogues are almost delocalised mixed-valent ions (borderline and Class III). Finally, despite their redox asymmetry, even in the heterobimetallic iron–rhodium *as*-indacenediide complexes, strong metal–metal coupling is present. In fact, oxidation of the iron centre is accompanied by electron transfer from rhodium to iron and formation of a reactive 17-electron rhodium site. *syn* and *anti* Fe–Rh *as*-indacenediide complexes are rare examples of heterobimetallic systems which can be classified as borderline Class II/Class III species.

Keywords: cyclopentadienyl ligands · iron · metal–metal interactions · mixed-valent compounds · rhodium

Introduction

Intramolecular electron transfer is one of the most important chemical processes. A tremendous effort has been and currently is devoted to the study of organometallic molecules in which two metal centres are located in close proximity and connected by an organic spacer.[1,2] Electronic coupling may significantly modify the individual properties or results in the development of novel characteristics which are not present in the monometallic compounds. Indeed, it is often sufficient to vary through simple reactions either the nature of the ancillary ligands of the metals or their redox state in order to induce new chemical and physical properties in the system.[3]

The greatest attention has been paid to complexes in which two equivalent metal moieties are bound through a hydrocarbon bridge, that is, homobimetallic complexes, whereas much less has been dedicated to heterobimetallic complexes.[1c,n,3j,m,4a]

In complexes in which two transition metals are anchored to two cyclopentadienyl (Cp) rings, a variety of spacers connect the two Cp rings,[1d,n] in the most prominent of which the two rings are 1) directly linked by a σ bond (fulvalenyl);[4] 2) separated by saturated linkers $-XR_2-$ (X = C, Si, Ge);[5] 3) connected by unsaturated $-(CH{=}CH)_n-$[6] or $-(C{\equiv}C)_n-$[7] chains (molecular wires) or arylene groups −Ar−;[8] and 4) fused in rigid polycyclic aromatic systems (pentalene,[1n,9a–c,g] indacene,[1n,9d–h] dicyclopentanaphtalene[9i–k] dianions, etc.).

In bimetallic complexes and corresponding mixed-valent derivatives, exact knowledge of the geometric metal–metal distance r_g is essential for interpreting electron-transfer phenomena.[1j,3a,10] Owing to the flexibility of bimetallic complexes containing spacers of types 1–3 the intermetallic distance is not certain, because in solution the complexes may

[a] Prof. S. Santi, Dr. L. Orian, Dr. C. Durante, Dr. E. Z. Bencze, A. Bisello, A. Donoli, Prof. A. Ceccon
Dipartimento di Scienze Chimiche
Università degli Studi di Padova
via Marzolo 1, 35131 Padova (Italy)
Fax: (+39) 049-827-5239
E-mail: saverio.santi@unipd.it

[b] Dr. F. Benetollo, Dr. L. Crociani
CNR, Istituto di Chimica Inorganica e delle Superfici
Corso Stati Uniti 4, 35127 Padova (Italy)

Supporting information (alternative synthesis of *syn*-**Fe_2** and *anti*-**Fe_2**; ^{1}H NMR spectra of *syn*-/*anti*-**Rh_2**, *syn*-/*anti*-**FeRh(cod)** and *syn*-**$FeRh(CO)_2$**; *xyz* coordinates of all the neutral and charged optimised complexes; and selected frontier orbitals of the neutral title compounds) for this article is available on the WWW under http://www.chemeurj.org/ or from the author.

assume different conformations than that adopted in the crystal structure. Moreover, when the linker is of type 2, it has been recently shown for a series of homobimetallic complexes that through-space electronic coupling may be of importance.[5a]

In contrast, in the case of fused polycyclic systems of type 4, the possibility of formation of stable *anti* and *syn* stereoisomers exists: in the former the two metal groups are located on opposite sides of the bridge, while in the latter the two metal units are on the same side. The rigidity of the bridging ligand causes the *syn* or *anti* configuration to be fixed, even in solution, because *syn–anti* isomerisation is difficult. The distance r_g ought to be different in the two stereoisomers,[11] whereas the true electron transfer distance r_{ab} may be equal to or shorter than r_g. Comparison between the two parameters is important to evaluate charge delocalisation in the whole complex.[10]

The results obtained for several bimetallic model complexes indicate that *s*- and *as*-indacenediide spacers (Scheme 1) are particularly effective in promoting metal–metal interaction.[9e,g]

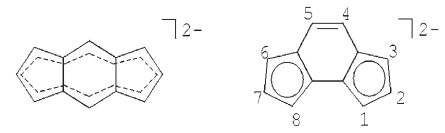

Scheme 1.

Among the homobimetallic compounds, those containing two FeCp redox centres are the most investigated, principally because of the stability of the neutral and oxidised species. Generally, however, results are restricted to complexes in which the two FeCp or FeCp* (Cp* = C_5Me_5) groups are located *anti* with respect to the plane of the indacenyl spacer, likely for steric reasons. Thus, information on the intramolecular communication in these important model compounds is limited to the *anti* stereoisomers.[9g,h] Consequently, the availability of *syn* and *anti* $(FeCp)_2$ indacenyl isomers is desirable for comparing the magnitude of the metal–metal electronic coupling in complexes which differ only in their stereochemistry.

Successful synthesis of pairs of stereochemical isomers is largely dependent on the synthetic procedure. A few years ago we succeeded in preparing mixtures of *syn* and *anti* isomers of *s*- and *as*-$(RhL_2)_2$-indacenediide complexes in which the relative percentage of the two isomers depends on the nature of the ancillary ligand L.[9f]

Here we report on rhodium–rhodium electronic coupling in the corresponding mixed-valent cations. In addition, we have now prepared mixtures of *syn* and *anti as*-indacenediide-$(FeCp)_2$ isomers by a two step thermophotochemical synthesis that is effective in transferring two FeCp groups to the *as*-indacene dianion. Iron–iron electronic coupling was also investigated.

This contribution describes the results of cyclic voltammetry and near- and mid-IR spectroscopy of iron and rhodium indacenyl mixed-valent cations obtained by spectroelectrochemistry from the neutral precursors illustrated in Scheme 2 and Figure 1. The results for homobimetallic species are compared with those obtained for the heterobimetallic [FeCp(*as*-indacenediide)Rh(cod)] complexes to gain deeper insight into how the different disposition and nature

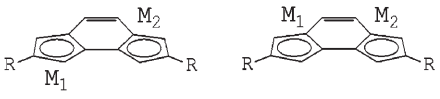

anti-**Fe_2**, *syn*-**Fe_2**	$M_1 = M_2$ = FeCp; R = H
anti-**Rh_2**, *syn*-**Rh_2**	$M_1 = M_2$ = Rh(cod); R = CH_3
anti-**FeRh(cod)**, *syn*-**FeRh(cod)**	M_1 = Rh(cod); M_2 = FeCp; R = H
anti-**FeRh$(CO)_2$**, *syn*-**FeRh$(CO)_2$**	M_1 = Rh$(CO)_2$; M_2 = FeCp; R = H

Scheme 2.

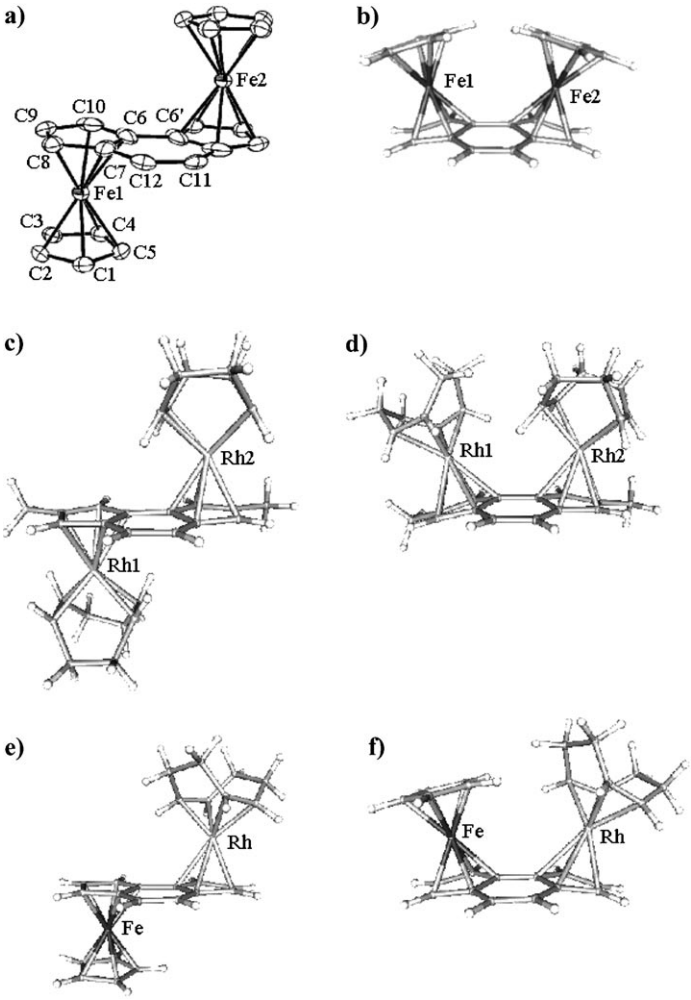

Figure 1. Molecular structures of a) *anti*-**Fe_2** (X-ray), b) *syn*-**Fe_2** (DFT optimised geometry), c) *anti*-**Rh_2** (X-ray),[9f] d) *syn*-**Rh_2** (X-ray),[9f] e) *anti*-**FeRh(cod)** (DFT optimised geometry) and f) *syn*-**FeRh(cod)** (DFT optimised geometry). Hydrogen atoms are not labelled for clarity.

of the metal moieties in the *syn* and *anti* isomers influence the degree of metal–metal electronic coupling.

Finally, the huge activation induced by oxidative electron transfer in the substitution of cod by two molecules of CO in the heterobimetallic [FeCp(*as*-indacenediide)Rh(cod)]$^+$ is discussed.

The experimental results are rationalised by a DFT analysis of neutral and charged iron and rhodium model complexes.

Results and Discussion

Synthesis and characterisation: The most frequently adopted procedure to prepare bimetallic [$(FeCp)_2$(μ-η^5:η^5-*as* and *s*-indacenediide)] complexes is the reaction of the indacenyl dianion with [Fe(acac)Cp][9g] (acac = acetylacetonate) or Cp^-/$FeCl_2$.[12] The net result is the sole formation of the *anti* isomer, while, to the best of our knowledge, the *syn* isomer was never isolated. We used a different approach which consists of two distinct thermal and photochemical steps. An efficient synthesis of [FeCp(η^5-indenyl)] complex was achieved some time ago through a sequence which proceeds through an initial thermal step providing the [$Fe(CO)_2$Cp(η^1-indenyl)] adduct[13a,b] followed by photochemical $\eta^1 \rightarrow \eta^5$ conversion with concurrent elimination of two molecules of CO.[13c,d] We adopted this method for transferring the FeCp unit to both Cp rings of the *as*-indacenediide ligand to give a *syn*/*anti* isomer mixture (Scheme 3).

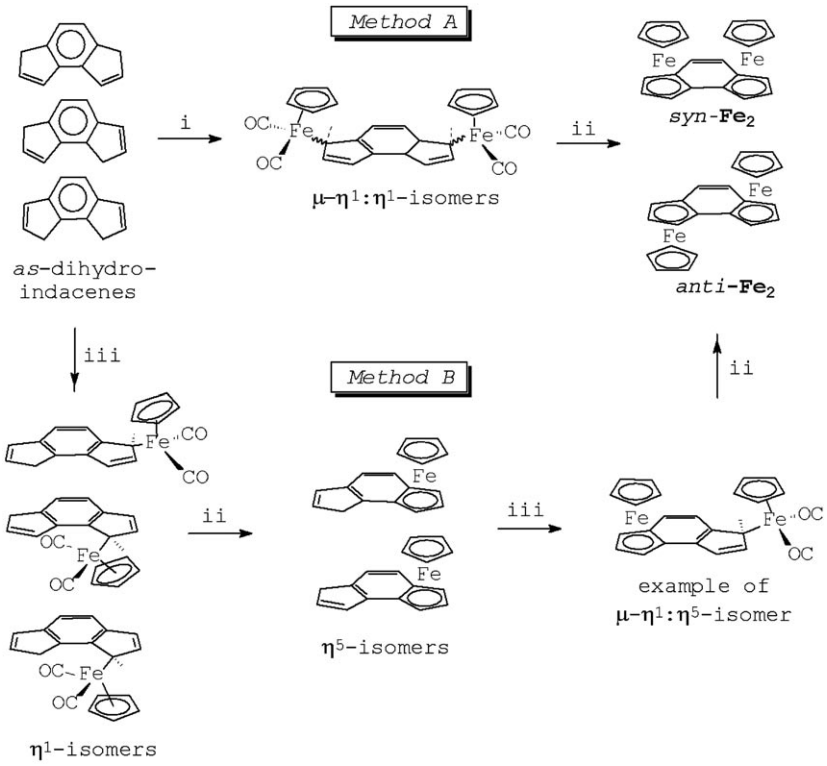

Scheme 3. Synthesis of *anti*-**Fe_2** and *syn*-**Fe_2**. i) 1. 2.2 equiv *t*BuLi in THF, $T = -50$ °C, 1 h; 2. 2 equiv of [$Fe(CO)_2$(Cp)I] in THF, -78 °C, 2 h. ii) *hv* in methylcyclohexane, $T = 20$ °C, 2 h. iii) 1. 1.1 equiv of *t*BuLi in THF, $T = -50$ °C, 1 h 30 min; 2. 1 equiv of [$Fe(CO)_2$(Cp)I] in THF, $T = -78$ °C, 3 h 30 min.

In the first step (Method A) double deprotonation of *as*-dihydroindacene followed by addition of [$Fe(CO)_2$(Cp)I] gave an mixture of [{$Fe(CO)_2$(Cp)}$_2$(μ-η^1:η^1-*as*-indacenediide)] isomers. Photochemical decarbonylation was monitored by IR spectroscopy until disappearance of the CO bands and formation of a 3:1 mixture of *anti*- and *syn*-[$(FeCp)_2$(μ-η^5:η^5-*as*-indacenediide)] isomers (*anti*-**Fe_2** and *syn*-**Fe_2**). Purification by chromatography yielded the pure *anti* isomer and a 1:1.5 mixture of *anti* and *syn* isomers, as shown by the ^{1}H NMR spectrum (Figure 2). In an alternative synthetic sequence (Method B of Scheme 3), stepwise addition of two FeCp units was employed (see the Supporting Information).

The spectra of *anti*-**Fe_2** and *syn*-**Fe_2** are similar but slightly shifted relative to each other. In particular, the Cp protons of the *syn* isomer are shifted downfield with respect to those

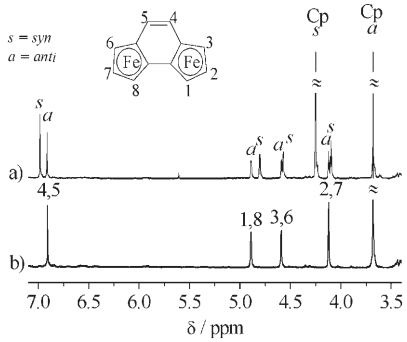

Figure 2. ^{1}H NMR spectra in $(CD_3)_2CO$ of a) 1.5:1 mixture of *syn*-**Fe_2** and *anti*-**Fe_2** and b) *anti*-**Fe_2**.

of the *anti* isomer due to the effect of magnetic anisotropy of the ring current induced by one Cp ring on the adjacent one. The X-ray structure of the *anti* isomer (Figure 1a) allowed univocal determination of its stereochemistry and identification of the ^{1}H NMR signals of both isomers.

The syntheses of *anti*-[{Rh(cod)}$_2$(μ-η^5:η^5-2,7-dimethyl-*as*-indacenediide)] (*anti*-**Rh_2**),[9f] *syn*-[{Rh(cod)}$_2$(μ-η^5:η^5-2,7-dimethyl-*as*-indacenediide)] (*syn*-**Rh_2**),[9f] *anti*-[FeCp(μ-η^5:η^5-*as*-indacenediide)Rh(cod)] (*anti*-**FeRh(cod)**)[9e] and *syn*-[FeCp(μ-η^5:η^5-*as*-indacenediide)Rh(cod)] (*syn*-**FeRh(cod)**) were previously described.[9e] In the case of *syn*-**Rh_2** and *anti*-**Rh_2** the *syn*:*anti* ratio depends on the nature of the an-

Table 1. Electrochemical data.[a,m]

Entry	Complex	E^1_p	E^2_p	$E^1_{1/2}$	$E^2_{1/2}$	$E^1_p-E^1_{p/2}$	$E^2_p-E^2_{p/2}$	$\Delta E_{1/2}$	K_c
i	*anti*-**Fe_2**[b]	0.147	0.785	0.116	0.756	0.061	0.058	0.640	9.3×10^{10}
ii	*anti*-**Fe_2**[c,e]	0.279	0.764	0.248	0.735	0.063	0.059	0.487	2.4×10^{8}
iii	*syn*-**Fe_2**/*anti*-**Fe_2**[b]	0.129	0.759	0.099	0.730	0.060	0.059	0.630	7.0×10^{10}
iv	*syn*-**Fe_2**/*anti*-**Fe_2**[c,f]	0.292	0.764	0.261	0.735	0.063	0.059	0.475	1.5×10^{8}
v	*anti*-**Rh_2**[b,g]	0.26	0.65	–	–	–	–	0.39[h]	5.1×10^{6}
vi	*syn*-**Rh_2**[b,g]	0.087	0.415	0.052	–	0.070	–	0.328[h]	4.4×10^{5}
vii	*anti*-**Rh_2**/*syn*-**Rh_2**[c]	0.380	0.190	0.345	0.143	0.070	0.094	0.190	1.8×10^{3}
viii	*syn*/*anti*-**FeRh(cod)**[b,i]	0.173	0.870	0.136	0.815	0.075	0.110	−0.556	–
ix	*syn*/*anti*-**FeRh(cod)**[c]	0.232	0.786	0.197	0.753	0.070[i]	0.067[i]		3.3×10^{9}
x	*syn*/*anti*-**$FeRh(CO)_2$**[c]	0.355	1.121	0.317	–	0.075	–[k]	–	–
xii	*anti*-**FeRh(cod)**[d,j]	0.420	0.920	0.380	–	0.074	–	0.500[h]	3.9×10^{8}
xiii	*syn*/*anti*-**$FeRh(CO)_2$**[d,j]	0.544	1.039	0.502	–	0.080[l]	–[l]	–	–

[a] Solvent CH_2Cl_2, scan rate 0.5 Vs^{-1} unless otherwise indicated; all potential are in volts relative to SCE; $T=20\,°C$; $E_{p/2}$ is the half-peak potential; $E_{1/2}=(E_p+E_{p/2})/2$; $\Delta E_{1/2}=E^2_{1/2}-E^1_{1/2}$; K_c is the comproportionation constant for the equilibrium given in Equation (1). Supporting electrolyte 0.1 mol dm^{-3}: [b] $nBu_4NB(C_6F_5)_4$, [c] nBu_4NPF_6, [d] nBu_4NBF_4. [e] At a scan rate of 50 Vs^{-1}. [f] At a scan rate of 5 Vs^{-1}. [g] At a scan rate of 0.1 Vs^{-1}. [h] ΔE_p value. [i] At a scan rate of 20 Vs^{-1}. [j] In THF.[9f] [k] $E^2_{pa}-E^2_{pc}=0.276$ V. [l] $E^2_{pa}-E^2_{pc}=0.195$ V. [m] The oxidation waves of entries i–iv, vi and ix–xii are fully reversible ($i_{pc}/i_{pa}\geq0.95$) determined by means of the Nicholson expression (*Anal. Chem.* **1965**, *37*, 1351), as are the first waves of entries vii, viii and xi. The second waves of entries vii and viii have i_{pc}/i_{pa} of 0.8 and approximately 0, respectively, while for entry v the current ratios were not determined (see Figure 3e).

cillary ligand L, and is in favour of the *syn* isomer (2:1) when L is cod.

The FeCp-transfer procedure adopted for *anti*-**Fe_2** and *syn*-**Fe_2** was used for the preparation of *syn*-**FeRh(cod)** and *anti*-**FeRh(cod)**.[9e]

In the iron–rhodium complexes substitution of cod with CO under mild conditions (20 °C, 1 atm) failed and the carbonylated product was obtained under more forcing conditions (50 °C, 10 atm). In contrast, in *anti*-**Rh_2** and *syn*-**Rh_2** cod could be easily displaced by CO even at −78 °C.[9f] It appears, therefore, that in the heterobimetallic complexes the presence of one FeCp group switches off the substitution reaction at rhodium.[9e] As significant electronic coupling has been observed for *anti*-**FeRh(cod)$^+$**[9e] we tried to promote the reaction by oxidative activation by adding an equimolar amount of $[Fe(C_5H_4COMe)(Cp)]BF_4$ to a 1:1 *syn*:*anti* mixture in dichloromethane saturated with CO at −25 °C. The aim was to generate the radical cation, which is expected to be more reactive with respect to the substitution of cod in an associative path. In fact, substitution of cod by two CO molecules, monitored by IR and ^1H NMR spectroscopy, took place to give the neutral *anti*-**$FeRh(CO)_2$**, identified by comparison with an authentic sample. Unexpectedly, only traces of *syn*-**$FeRh(CO)_2$** were present.[15]

The carbonylation reaction may also proceed quantitatively and rapidly by using trace amounts of the oxidant. This indicates that oxidation leads to rapid and efficient cod substitution by an electron-transfer-catalysed (ETC)[16] pathway to afford *anti*-**$FeRh(CO)_2$**. Under the same conditions the reaction was also carried out in an IR-spectroelectrochemical experiment with nBu_4NPF_6 as supporting electrolyte. Initial appearance of the carbonyl stretching bands of *anti*-**$FeRh(CO)_2$** was recorded when oxidation was maintained at the onset potential of the first wave (see Table 1 for electrochemical data).

These results clearly indicate that, in the carbonylation of *syn*- and *anti*-**FeRh(cod)**, catalytic activation by oxidative electron transfer must be accompanied by *syn–anti* isomerisation. The ETC process can be rationalised by comparing the oxidation potentials (Table 1): the carbonyl complexes are oxidised at a potential 130 mV more positive than the cod complexes. Consequently, *syn*- and *anti*-**$FeRh(CO)_2^+$** can oxidise the starting complexes and are themselves reduced in the catalytic cycle depicted in Scheme 4.

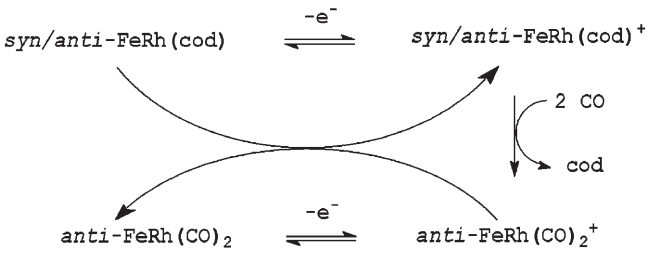

Scheme 4.

Notably, *syn*-to-*anti* isomerisation is a rarely observed process.[11] We showed that carbonylation of neutral *syn*-**Rh_2**/*anti*-**Rh_2** mixture takes place with retention of configuration and isomer ratio.[9f] Therefore, the oxidative conditions appear to be responsible for isomerisation. As previously reported for heterobimetallic $[Cr(CO)_3(\mu\text{-}\eta\text{:}\eta\text{-indenyl})Rh(nbd)]$ (nbd = norbornadiene) a similar isomerisation takes place, but only in the presence of catalytic amounts of ML_2^+ cations.[11b]

^{103}Rh NMR spectroscopy: Coupling of the ^{103}Rh nucleus with the protons of cod in *syn*-**Rh_2**,[17] *anti*-**Rh_2**,[17] *anti*-**FeRh(cod)** and *syn*-**FeRh(cod)**, and with H2 in *anti*-**$FeRh(CO)_2$** and *syn*-**$FeRh(CO)_2$**, enabled the measurement of ^{103}Rh chemical shifts (Table 2). The $\delta(^{103}Rh)$ values of all the complexes are typical of η^5 coordination of the Cp ring.[17] More interestingly, the chemical shifts of the *syn* complexes al-

Table 2. ^{103}Rh NMR chemical shifts.[a,b]

Complex	$\delta(^{103}Rh)$ [ppm]
***anti*-Rh$_2$**	−552[c]
***syn*-Rh$_2$**	−457[c]
***anti*-FeRh(cod)**	−598
***syn*-FeRh(cod)**	−481
***anti*-FeRh(CO)$_2$**	−1119
***syn*-FeRh(CO)$_2$**	−1081

[a] $T=300$ K. [b] [D$_6$]acetone. [c] CD_2Cl_2.

lowed assignment of the metal configuration of the *syn* and *anti* heterobimetallic isomers. In fact, as observed for the ^{1}H chemical shift of C_5H_5 in the spectra of ***anti*-Fe$_2$** and ***syn*-Fe$_2$**, the $\delta(^{103}Rh)$ of *syn* complexes are shifted downfield with respect to those of the *anti* isomers due to the effect of the magnetic anisotropy of the nuclear electronic current induced by one rhodium group on the adjacent one.

Electrochemical data: The anodic behaviour of all the complexes investigated (Table 1) in cyclic voltammetry (CV) experiments in CH_2Cl_2/0.1 mol dm^{-3} nBu$_4$NPF$_6$ in the range of potential scan rates of $0.1<v<50$ V s^{-1}, displays two one-electron waves which, except for ***anti*-Fe$_2$**, are fully reversible in the Nernstian and chemical senses (Figure 3a–c).

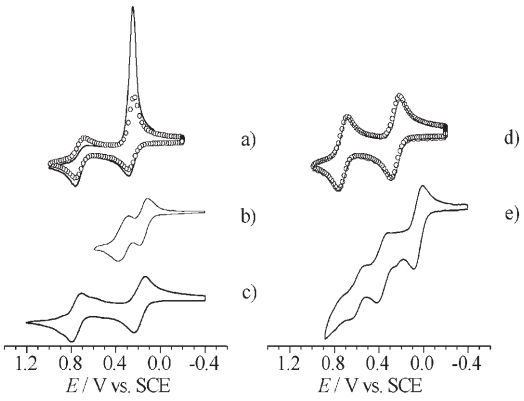

Figure 3. Cyclic voltammograms in CH_2Cl_2 at a gold disc electrode (diameter 0.5 mm), $T=20$ °C: a) 3.0×10^{-3} mol dm^{-3} ***anti*-Fe$_2$** (line) and 1:1 mixture of 2.9×10^{-3} mol dm^{-3} ***anti*-Fe$_2$** and ***syn*-Fe$_2$** (open circles) with 0.1 mol dm^{-3} nBu$_4$NPF$_6$, scan rate $v=0.5$ V s^{-1}; b) 2:1 mixture of 2.5×10^{-3} mol dm^{-3} ***anti*-Rh$_2$** and ***syn*-Rh$_2$**, scan rate $v=0.5$ V s^{-1}; c) 1:1 mixture of 8.4×10^{-3} mol dm^{-3} ***anti*-FeRh(cod)** and ***syn*-FeRh(cod)**, scan rate $v=0.5$ V s^{-1}; d) 3.0×10^{-3} mol dm^{-3} ***anti*-Fe$_2$** (line) and 1:1 mixture of 1.8×10^{-3} mol dm^{-3} ***anti*-Fe$_2$** and ***syn*-Fe$_2$** (open circles) with 0.1 mol dm^{-3} nBu$_4$NB(C$_6$F$_5$)$_4$, scan rate $v=0.5$ V s^{-1}; e) 2:1 mixture of 3.0×10^{-3} mol dm^{-3} ***anti*-Rh$_2$** and ***syn*-Rh$_2$** with 0.1 mol dm^{-3} nBu$_4$NB(C$_6$F$_5$)$_4$, scan rate $v=0.1$ V s^{-1}.

The second oxidation wave of ***anti*-Fe$_2$** in fact corresponds to a chemically irreversible and not a diffusion-controlled process at potential scan rates below 50 V s^{-1} with a typical stripping peak as cathodic counterpart of the first wave. This indicates that the dication ***anti*-Fe$_2^{2+}$** produced at the second wave precipitates on the gold electrode.

The cyclic voltammetry of a 1:1 mixture of ***anti*-Fe$_2$** and ***syn*-Fe$_2$** exhibits oxidation potentials almost identical to those of a pure sample of ***anti*-Fe$_2$**, and this suggests that the thermodynamic features of the two isomers are equivalent. At lower concentrations of ***anti*-Fe$_2^{2+}$**, the stripping peak is less pronounced and disappears at lower scan rate (5 V s^{-1}). In contrast, the oxidation of ***syn*-Fe$_2$** is predominantly a diffusion-controlled process.

Using nBu$_4$NB(C$_6$F$_5$)$_4$ (Figure 3d) increases the solubility of ***anti*-Fe$_2^{2+}$**, and the corresponding redox process becomes diffusion-controlled and fully reversible. Interestingly, the separations $\Delta E_{1/2}$ between the two one-electron waves of pure ***anti*-Fe$_2$** and of the isomer mixture increase by 150 mV when the anion is changed from BF_4^- to $B(C_6F_5)_4^-$. The $\Delta E_{1/2}$ values are almost identical (640 and 630 mV, respectively; Table 1), so that the stabilities of ***anti*-Fe$_2^+$** and ***syn*-Fe$_2^+$** are approximately the same. In fact, the $\Delta E_{1/2}$ value allows determination of ΔG_c and of the related comproportionation constant K_c (Table 1) for the equilibrium given in Equation (1).

$$[M_1\text{-}M_2] + [M_1{}^+\text{-}M_2{}^+] \rightleftharpoons 2\,[M_1\text{-}M_2]^+ \quad (1)$$

Large values of K_c and $\Delta E_{1/2}$ are essential requirements for isolation of a complex in its mixed-valent state, and the order of magnitude of K_c (ca. 10^{11}) found for ***anti*-Fe$_2^+$** and ***syn*-Fe$_2^+$** is indicative of their high thermodynamic stability with respect to disproportionation.[2]

For the ***syn*-Rh$_2$** and ***anti*-Rh$_2$** isomers, available in a 2:1 mixture, CV experiments in CH_2Cl_2/nBu$_4$NPF$_6$ in the same range of potential scan rates revealed only two reversible waves (Figure 3b). However, in CH_2Cl_2/nBu$_4$NB(C$_6$F$_5$)$_4$ four reversible redox features appear in the anodic scan (Figure 3e). The relative intensities of the waves enable assignment of the potential values to the corresponding isomers. Oxidation of ***anti*-Rh$_2$** occurs at more positive potential than that of ***syn*-Rh$_2$**. The $\Delta E_{1/2}$ between the two one-electron waves increases by 200 and 140 mV, respectively, when the anion is changed from BF_4^- to $B(C_6F_5)_4^-$. As for the diiron isomers, the $\Delta E_{1/2}$ values (390 and 330 mV, respectively; Table 1) are moderately susceptible to the stereochemical disposition of the Rh(cod) groups; the K_c values of ***anti*-Rh$_2$** and ***syn*-Rh$_2$** decrease from 5.1×10^6 to 4.4×10^5. These values are much lower than those of ***anti*-Fe$_2$** and ***syn*-Fe$_2$** isomers.

The appearance of new waves in the CV of Figure 3e is due to the different sensitivities of ***anti*-Rh$_2$** and ***syn*-Rh$_2$** to changing the electrolyte anion from PF_6^- to $B(C_6F_5)_4^-$. In fact, there is evidence that traditional anions such as BF_4^- and PF_6^- may react as nucleophiles with radical cations.[19a] Weakly coordinating anions with highly delocalised negative charges, such as $B(C_6F_5)_4^-$, allow nucleophilic attack on the radical cations to be minimised. In addition, they undergo much weaker ion pairing than the traditional anions in low-polarity solvents. These properties make it possible to manipulate the anodic $\Delta E_{1/2}$ values, and the largest values are obtained in less polar solvents with low donor number.[19a] In the case of ***anti*-Rh$_2$** and ***syn*-Rh$_2$**, the variation of the electrolyte anion not only modifies the comproportionation thermodynamics of the redox equilibrium of Equation (1),

Table 3. NIR data.[a]

Cation	$\tilde{\nu}_{max}$ [b] [cm^{-1}]		ε_{max} [$mol^{-1}\,dm^3\,cm^{-1}$]	ΔG_0 [cm^{-1}]	$(\Delta\tilde{\nu}_{1/2})_{obsd}$ [cm^{-1}]	$(\Delta\tilde{\nu}_{1/2})_{calcd}$ [cm^{-1}]	H_{ab} [cm^{-1}]	α	$\Delta G^{\neq}$ [$kJ\,mol^{-1}$]	Γ
anti-$\mathbf{Fe_2}^+$	(13840)	5025	765	–	2860	3130	430	0.085	72.4	0.09
syn-$\mathbf{Fe_2}^+$	(13270)	7170	395	–	3590	3740	460	0.064	114.0	0.04
anti-$\mathbf{Rh_2}^+$[c]	–	6485	5175	–	1350	3560	3240[d]	0.5	–	0.62
syn-$\mathbf{Rh_2}^+$	(11360)	8660	2070	–	1830	4110	4330[d]	0.5	–	0.56
syn-$\mathbf{Rh_2}^+$[c]	(11100)	8500	3790	–	2160	4070	4250[d]	0.5	–	0.47
syn,anti-$\mathbf{FeRh(cod)}^+$	(18400)	6725	8065	4480	1960	3620	3360[d]	0.5	–	0.46
anti-$\mathbf{FeRh(cod)}^+$[e]	–	7580	2570	4030	2020	3380	3790[d]	0.5	–	0.40
syn,anti-$\mathbf{FeRh(CO)_2}^+$	–	8790	2850	[f]	2070	–	–	–	–	–

[a] Solvent was CH_2Cl_2/n-Bu_4NPF_6, $T=-20\,°C$; [b] $\pm 4\ cm^{-1}$; values in parentheses are band energies in the visible region. [c] With n-$Bu_4NB(C_6F_5)_4$ as supporting electrolyte. [d] Minimum value calculated by using equation $H_{ab}=\tilde{\nu}_{max}/2$. [e] At -78 K in THF/n-Bu_4NBF_4.[9f] [f] Not measured due to irreversibility of the second wave.

but also enables us to distinguish the *syn* and *anti* isomers by mean of their oxidation potentials.

For the sake of comparison, we measured the anodic characteristics of a 1:1 mixture of *anti*-**FeRh(cod)** and *syn*-**FeRh(cod)** in $CH_2Cl_2/0.1\ mol\,dm^{-3}$ n-Bu_4NPF_6 (Figure 3c). Their electrochemical and optical analyses in a different medium (THF/$0.1\ mol\,dm^{-3}$ n-Bu_4NBF_4) were previously reported by us. Under those conditions the oxidation waves of the two isomers were clearly different, whereas in CH_2Cl_2/n-Bu_4NPF_6 only two one-electron waves appeared, the second of which became chemically irreversible with n-$Bu_4NB(C_6F_5)_4$ as supporting electrolyte. Thus, in CH_2Cl_2/n-Bu_4NPF_6 the two heterobimetallic isomers exhibit almost identical electrochemical behaviour, as in the case of diiron and dirhodium isomers. The values (Table 1) of $\Delta E_{1/2}$ (560 mV) and K_c (3.3×10^9) are close to those found for the diiron complexes, and this suggests that the presence of at least one FeCp group coordinated to the *as*-indacenediide ligand confers quite similar stability towards disproportionation of the corresponding bimetallic cations [Eq. (1)].

The values of K_c and $\Delta E_{1/2}$ determined by electrochemical measurements have been widely used for assessing the degree of electronic coupling in mixed-valent complexes. However, the electronic-coupling parameters derived from classical and semiclassical theoretical models[2a,b,h,k] and from electrochemical studies are frequently in poor agreement.[19] As previously reported[19] and also shown here, caution is needed in the interpretation of electrochemical data due to the considerable dependence of redox potential and reversibility on the nature of the solvent and supporting electrolyte. Much better results and agreement with the theoretical treatment are usually provided by optical investigations in the near-IR region where mixed-valent species typically absorb.

Near-IR analysis: The mixed-valent cations of homo- and heterobimetallic Fe–Fe, Rh–Rh and Fe–Rh complexes in both *syn* and *anti* configurations have been investigated in the near-IR, where they display a characteristic intervalence transition (IT) band. Particular attention is devoted to determining how the different nature and the stereochemical disposition of the metal groups influence the degree of the metal–metal electronic coupling.

The degree of electronic coupling H_{ab} between M_1 and M_2 determines the class of a mixed-valent system in the Robin and Day scheme.[2c] A system belongs to Class I when the metal centres are far apart or the M_1–M_2 interaction is symmetry- or spin-forbidden ($H_{ab}=0$). In Class II systems the electronic coupling between M_1 and M_2 is weak or moderate and transfer of a unit charge λ (the reorganisation energy) occurs ($2H_{ab}\ll\lambda$). In Class III systems electronic coupling is strong and the valence of the metals is delocalised ($2H_{ab}\gg\lambda$); the transition does not involve net charge transfer and the system is better defined as an "average valence".[2l]

In the Class II regime the IT bands in the near-IR region are weak and broad and the transition energy $h\nu$ is equal to λ. The magnitude of H_{ab} and of the activation energy of the thermal electron transfer ($\Delta G^{\neq}$) are related to the energy $\tilde{\nu}_{max}$, intensity ε_{max}, and half-bandwidth $(\Delta\tilde{\nu}_{1/2})_{obsd}$ of the IT absorption through the two-state, classical Marcus–Hush theory.[2a,b] The predicted $(\Delta\nu_{1/2})_{Hush}$ is given by Equations (2) and (3), in which the redox asymmetry ΔG_0 is the energy difference between the two states M_1^+-spacer-M_2 and M_1-spacer-M_2^+ estimated from the $E_{1/2}$ values (Table 3 and Table 4), λ the reorganisation energy and $\tilde{\nu}_{max}$ the energy required for optical electron transfer (E_{op}).

$$(\Delta\tilde{\nu}_{1/2})_{Hush}\ [cm^{-1}] = [16\,RT\ln 2\,\lambda]^{1/2} \quad (2)$$

$$\lambda = \tilde{\nu}_{max} - \Delta G_0 \quad (3)$$

The near-IR spectrum of pure *anti*-$\mathbf{Fe_2}$ in $CH_2Cl_2/0.1\ mol\,dm^{-3}$ n-Bu_4NBPF_6 (Figure 4a, Table 3), obtained in a spectroelectrochemical experiment at applied potentials

Table 4. Solvent effects on the IT band for *anti*-$\mathbf{Rh_2}^+$ and *syn*-$\mathbf{Rh_2}^+$.

	THF	CH_2Cl_2	CH_3CN
ε_r[a]	7.52	9.1	35.9
DN[b]	21	1	14.6
$(1/n^2)-(1/\varepsilon_o)$[c]	0.372	0.382	0.526
$\tilde{\nu}_{max}$(*anti*-$\mathbf{Rh_2}^+$)[d]	5480	6485	6325
$\tilde{\nu}_{max}$(*syn*-$\mathbf{Rh_2}^+$)[d]	8240	8660	8820

[a] Relative permittivity (dielectric constant).[20] [b] Donor number.[20] [c] n is the refractive index.[20] λ ($=\tilde{\nu}_{max}$) is predicted to be linear with $1/n^2-1/\varepsilon_r$ by the classical two-state Hush theory.[2a,b] [d] $\tilde{\nu}_{max}$ in cm^{-1} ($\pm 4\ cm^{-1}$).

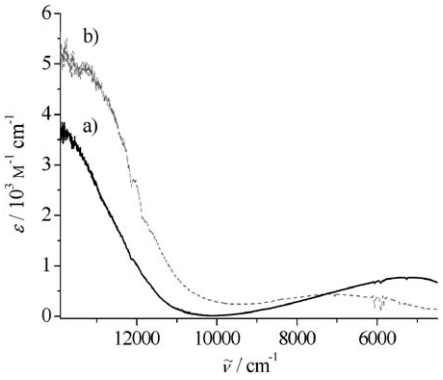

Figure 4. Near-IR spectroelectrochemistry at −25 °C and at applied potentials from 0.2 to 0.4 V ($v=5$ mV s^{-1}) of 3.0×10^{-3} mol dm^{-3} *anti*-**Fe$_2$** (line) and of 1.45×10^{-3} mol dm^{-3} *anti*-**Fe$_2$** and *syn*-**Fe$_2$** (dotted line) with 0.1 mol dm^{-3} nBu$_4$NPF$_6$.

from 0.2 to 0.4 V ($T=-25$ °C, scan rate $v=5$ mV s^{-1}), showed the appearance of a weak Gaussian-shaped absorption band at 5025 cm^{-1} ($\varepsilon_{max}=765$ mol^{-1} dm^3 cm^{-1}).

Under the same conditions, a 1:1 mixture of *anti*-**Fe$_2$** and *syn*-**Fe$_2$** exhibited a broad and less intense band whose deconvolution evidenced the presence of two distinct absorptions corresponding to *anti*-**Fe$_2$**$^+$ and, at higher energy, *syn*-**Fe$_2$**$^+$. By subtracting the absorption of the *anti* isomer from the spectrum of the mixture, a well-defined band of the *syn*-**Fe$_2$**$^+$ isomer (Figure 4, Table 3) was obtained at 7170 cm^{-1} ($\varepsilon_{max}=395$ mol^{-1} dm^3 cm^{-1}). Both of these bands are IT transitions typical of localised Class II mixed-valent species. In fact, the experimental half-bandwidths of the two isomers ($(\Delta\tilde{\nu}_{1/2})_{obsd}=2860$ and 3590 cm^{-1}) and the calculated values ($(\Delta\tilde{\nu}_{1/2})_{calcd}=3131$ and 3740 cm^{-1}) are quite similar. Brunschwig, Creutz and Sutin proposed a criterion based on the observed and calculated half-bandwidths,[2k] according to Equation (4).

$$\Gamma = 1-(\Delta\tilde{\nu}_{1/2})_{obsd}/(\Delta\tilde{\nu}_{1/2})_{calcd} \quad (4)$$

The magnitude of Γ enables classification of a mixed-valent species: $0<\Gamma<0.1$ for weakly coupled Class II systems, $0.1<\Gamma<0.5$ for moderately coupled Class II systems, $\Gamma\approx0.5$ for borderline Class II/III systems and $\Gamma>0.5$ for delocalised Class III systems.

These results demonstrate that *anti*-**Fe$_2$**$^+$ ($\Gamma=0.088$) and *syn*-**Fe$_2$**$^+$ ($\Gamma=0.041$) are weakly coupled Class II systems. Thus, the electronic coupling H_{ab} can be calculated by the Hush equation [Eq. (5)].[2a,b]

$$H_{ab} = \frac{0.0205\,(\varepsilon_{max}\tilde{\nu}_{max}\Delta\tilde{\nu}_{1/2})^{1/2}}{r_{ab}} \quad (5)$$

Here r_{ab} is the true electron-transfer distance. When electronic coupling is significant, r_{ab} can be considerably shorter than the geometric distance r_g. By using the DFT computed iron–iron distances (Table 5) in *anti*-**Fe$_2$**$^+$ and *syn*-**Fe$_2$**$^+$ of 5.29 and 4.63 Å, respectively, we estimate the lower limits of H_{ab} to be 426 and 459 cm^{-1}. The delocalisation coefficients α, defined in Equation (6), of 0.085 and 0.064 indicate that the degree of valence delocalisation in the ground state (i.e., the fraction of valence electronic charge transferred) is small and only slightly different in the two isomers. More accurate values of H_{ab} should be obtainable by estimating the true distance r_{ab}.[3a,10a] However, if r_{ab} in *anti*-**Fe$_2$**$^+$ and *syn*-**Fe$_2$**$^+$ were significantly shorter than r_g, the revised H_{ab} values should still be close to those expected for a moderate metal–metal interaction, according to the Γ values and the weakness of the IT bands. In addition, in Class II systems electron transfer can occur by thermal activation and the activation energy $\Delta G^{\neq}$ is given by Equation (7),[2h,k] which provides $\Delta G^{\neq}$ of 72.4 and 114.0 kJ mol^{-1} for *anti*-**Fe$_2$**$^+$ and *syn*-**Fe$_2$**$^+$, respectively.

$$\alpha = \frac{H_{ab}}{\tilde{\nu}_{max}} \quad (6)$$

$$\Delta G^{\neq} = \frac{\lambda}{4} - H_{ab} + \frac{H_{ab}^2}{\lambda} \quad (7)$$

These outcomes together with the Γ and α values reveal that electron transfer occurs slightly, but definitely more, efficiently when the FeCp groups are in an *anti* conformation despite the closer proximity of the two metals in the *syn* isomer. Hence, intramolecular electron transfer from Fe^{II} to Fe^{III} occurs mainly through the *as*-indacenediide bridge rather than through space.

Significantly different results are obtained on analysing the optical data of *anti*-**Rh$_2$**$^+$ and *syn*-**Rh$_2$**$^+$. As shown in Figure 3b and d, use of the opportune supporting electrolyte, that is, nBu$_4$NB(C$_6$F$_5$)$_4$, is crucial to selectively oxidise the *syn* isomer. Near-IR spectroelectrochemical experiments ($T=-25$ °C, scan rate $v=5$ mV s^{-1}) were carried out with a 2:1 mixture of *anti*-**Rh$_2$** and *syn*-**Rh$_2$** in CH$_2$Cl$_2$/0.1 mol dm^{-3} nBu$_4$NB(C$_6$F$_5$)$_4$. The potential was maintained at the onset value of the first wave corresponding to the *syn*-**Rh$_2$**$^{0/+}$ redox couple (Figure 5a and b; Table 3).

The spectrum displays a quite intense absorption band ($\tilde{\nu}_{max}=8500$ cm^{-1}, $\varepsilon_{max}=3790$ mol^{-1} dm^3 cm^{-1}) and a second absorption at higher energy ($\tilde{\nu}_{max}=11\,100$, $\varepsilon_{max}=2600$ mol^{-1} dm^3 cm^{-1}). On increasing the applied potential to the value corresponding to the *anti*-**Rh$_2$**$^{0/+}$ redox couple, a third more intense and narrower band appears at lower energy (Figure 5c–f and h; Table 3; $\tilde{\nu}_{max}=6485$ cm^{-1}, $\varepsilon_{max}=5175$ mol^{-1} dm^3 cm^{-1}). The discrepancy between the experimental and calculated half-bandwidths, $(\Delta\tilde{\nu}_{1/2})_{obsd}=2160$ and $(\Delta\tilde{\nu}_{1/2})_{calcd}=4070$ cm^{-1} for *syn*-**Rh$_2$**$^+$, 1350 and 3560 cm^{-1} for *anti*-**Rh$_2$**$^+$, requires that these two isomeric cations are not weakly coupled Class II mixed-valent species and that the electronic coupling H_{ab} cannot be calculated by Equation (5). Moreover, the values of Γ (Table 3) obtained for *syn*-**Rh$_2$**$^+$ (0.47–0.56) and *anti*-**Rh$_2$**$^+$ (0.62) reveal that *syn*-**Rh$_2$**$^+$ is an almost delocalised borderline Class II/III system,

Table 5. Selected interatomic distances [Å] and angles [°] of *anti*-$\mathbf{Fe_2}^{0/+}$, *syn*-$\mathbf{Fe_2}^{0/+}$, *anti*-$\mathbf{H\text{-}Rh_2}^{0/+}$, *syn*-$\mathbf{H\text{-}Rh_2}^{0/+}$, *anti*-$\mathbf{FeRh(cod)}^{0/+}$ and *syn*-$\mathbf{FeRh(cod)}^{0/+}$. Where available, crystallographic data of similar complexes are given in italics.

	anti-$\mathbf{Fe_2}$		*anti*-$\mathbf{Fe_2}^+$[e]		*syn*-$\mathbf{Fe_2}$		*syn*-$\mathbf{Fe_2}^+$	
Fe1–Q1[a]	1.70	*1.656(7)*[f]	1.75	–	1.71	–	1.71	–
		1.64[g]	(1.72)	*1.70*[h]		–		–
Fe1–Q2[a]	1.68	*1.656(7)*[f]	1.76	–	1.69	–	1.69	–
		1.66[g]	(1.72)	*1.69*[h]		–		–
Fe2–Q1′[a]	1.70	*1.646(6)*[f]	1.70 (1.72)	–	1.71	–	1.76	–
		1.64[g]		*1.659*[h]		–		–
Fe2–Q2′[a]	1.68	*1.646(6)*[f]	1.68 (1.72)	–	1.69	–	1.77	–
		1.66[g]		*1.66*[h]		–		–
Fe1–Fe2	5.21	*5.081(2)*[f]	5.29 (5.24)	–	4.64	–	4.63	–
		5.12[g]		*5.14*[h]		–		–
Δ1,2[b]	0.019	*0.023*[f]	0.12, 0.019 (0.058,0.058)	–	0.069, 0.073	–	0.040, 0.157	–
		0.043[g]		0.039[h]		–		–
FA_{Cp}1,2[c]	0.6	*0.0*[f]	3.6, 2.2 (2.7, 2.7)	–	0.9, 0.9	–	1.0, 1.8	–
		0.0[g]		*0.0*[h]		–		–
BA_{ind}1,2[d]	0.1	*0.0*[f]	1.3, 1.3 (2.3, 2.3)	–	10.0, 10.0	–	8.2, 7.8	–

	anti-$\mathbf{H\text{-}Rh_2}$		*anti*-$\mathbf{H\text{-}Rh_2}^+$		*syn*-$\mathbf{H\text{-}Rh_2}$		*syn*-$\mathbf{H\text{-}Rh_2}^+$	
Rh1–Q1[a]	2.01	*1.92*[i]	1.98	–	2.03	*1.36*[j]	1.99	–
Rh2–Q2[a]	2.01	*1.92*[i]	1.98	–	2.05	*1.91*[j]	2.00	–
Rh1–Rh2	5.89	*4.29*[i]	5.73	–	5.22	*4.72*[j]	4.81	–
Δ1,2[b]	0.10	*0.00*[i]	0.11	–	0.27, 0.30	*0.082*, *0.12*[j]	0.19, 0.14	–
FA_{Cp}1,2[c]	9.9	*0.0*, *3.0*[i]	5.9, 5.9	–	11.5, 11.9	*2.5*, *2.5*[j]	7.7, 6.1	–
BA_{ind}1,2[d]	2.2	*0.0*, *0.0*[i]	2.8, 2.8	–	8.3, 8.9	*4.2*, *4.2*[j]	7.2, 7.7	–

	anti-FeRh(cod)		*anti*-FeRh(cod)$^+$		*syn*-FeRh(cod)		*syn*-FeRh(cod)$^+$	
Fe–Q1[a]	1.70	–	1.74	–	1.71	–	1.74	–
Fe–Q1′[a]	1.68	–	1.76	–	1.68	–	1.76	–
Rh–Q2[a]	2.00	–	2.02	–	2.04	–	2.06	–
Fe–Rh	5.53	–	5.59	–	4.84	–	4.82	–
Δ1,2[b]	0.055 (Fe)	–	0.12 (Fe)	–	0.067 (Fe)	–	0.13(Fe)	–
	0.16 (Rh)	–	0.15(Rh)	–	0.25 (Rh)	–	0.24(Rh)	–
FA_{Cp}1,2[c]	2.7(Fe)	–	4.9(Fe)	–	3.0(Fe)	–	5.4(Fe)	–
	8.4(Rh)	–	7.6(Rh)	–	10.1(Rh)	–	9.2(Rh)	–
BA_{ind}1,2[d]	1.7(Fe)	–	1.9(Fe)	–	5.5(Fe)	–	4.1(Fe)	–
	2.3(Rh)	–	2.4(Rh)	–	11.2(Rh)	–	9.0(Rh)	–

[a] Q1,2 denotes the centroids of the Cp moieties of the indacenyl ligand, and Q1′,2′ the centroids of the free Cp rings. [b] Slippage parameter.[22] [c] Folding angle of the Cp moieties of the indacenyl ligand.[22] [d] Bending angle of the indacenyl ligand. [e] Data in parentheses refer to the calculated higher energy structure with C_2 symmetry. [f] Crystallographic data of *anti*-[{Fe(C_5H_5)}$_2$(μ-η^5:η^5-*as*-indacenediide)] reported in this work. [g] Data from ref. [24]. [h] Data from ref. [25]. [i] Crystallographic data of *anti*-[{Rh(cod)}$_2$(μ-η^5:η^5-2,7-dimethyl-*as*-indacenediide)].[9f] [j] Crystallographic data of *syn*-[{Rh(cod)}$_2$(μ-η^5:η^5–2,7-dimethyl-*as*-indacenediide)].[9f]

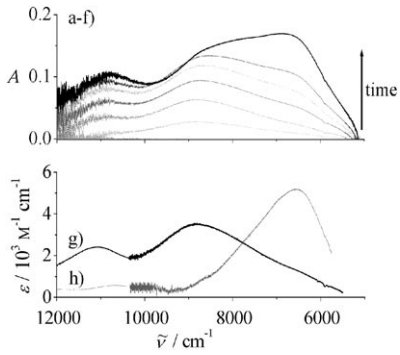

Figure 5. Near-IR spectroelectrochemistry at −25 °C and at applied potentials from 0.2 to 0.4 V (v = 5 mV s^{-1}) of a 2:1 mixture of 3.0 × 10^{-3} mol dm^{-3} *anti*-$\mathbf{Rh_2}$ and *syn*-$\mathbf{Rh_2}$ with 0.1 mol dm^{-3} nBu$_4$NB(C_6F_5)$_4$: a–f) time evolution, acquisition steps 30 s; g) spectrum of *syn*-$\mathbf{Rh_2}^+$; h) spectrum of *anti*-$\mathbf{Rh_2}^+$ obtained by subtracting the contribution of *syn* isomer from spectrum f).

whereas *anti*-$\mathbf{Rh_2}^+$ is better described as a delocalised Class III mixed-valent species.

The IT band energy $\tilde{\nu}_{max}$ of a delocalised mixed-valent system is expected to be solvent-independent.[2] We studied the solvent effect on the IT bands comparing $\tilde{\nu}_{max}$ values obtained in three different solvents (Table 4), namely, CH_2Cl_2, CH_3CN and THF.[20] For *syn*-$\mathbf{Rh_2}^+$ a moderate blue shift of $\tilde{\nu}_{max}$ was observed with an increase in the dielectric parameter ($1/n^2-1/\varepsilon_o$).[2a,b] Conversely, the IT band energy of *anti*-$\mathbf{Rh_2}^+$ in CH_2Cl_2 and CH_3CN, which have very different dielectric parameters and donor numbers, is almost constant. The large red shift observed on going from CH_2Cl_2 to THF, which have almost identical dielectric parameters, is in contrast to the expectation from Marcus–Hush and related non-equilibrium solvent polarisation theories. On the other hand, THF has a much higher donicity (DN = 21) than CH_2Cl_2 (DN = 1). We believe that in THF the dielectric-continuum approximation breaks down and specific solvent ef-

fects are present and responsible for the observed red shift.[2j]

The small half-bandwidths relative to the magnitude of Γ and the solvent effect confirm that *syn*-**Rh_2^+** and *anti*-**Rh_2^+** can be classified with good confidence as borderline and Class III species, respectively. In this case, *syn–anti* isomerism of the two Rh(cod) groups in *as*-indacenediide mixed-valent systems drives the borderline-to-Class III transition. To the best of our knowledge, *anti*-**Rh_2^+** is the first example of a delocalised, Class III, "average valence" cation of *as*-indacenediide.

Finally, we re-examined the heterobimetallic complexes *syn*-**FeRh(cod)** and *anti*-**FeRh(cod)** in CH_2Cl_2/n-Bu_4NBPF_6. Within the classical Hush theory the introduction of a redox asymmetry ΔG_0 into a binuclear system increases the energy barrier to thermal electron transfer and diminishes the extent of metal–metal electronic coupling. The near-IR spectrum obtained by oxidising a 1:1 mixture of *syn*-**FeRh(cod)** and *anti*-**FeRh(cod)** in a spectroelectrochemical experiment displayed an intense and narrow band (Figure 6, Table 3: $\tilde{\nu}_{1/2} = 6725\ cm^{-1}$, $\varepsilon_{max} = 8065\ mol^{-1}\,dm^3\,cm^{-1}$, $(\Delta\tilde{\nu}_{1/2})_{obsd} = 1960\ cm^{-1}$).

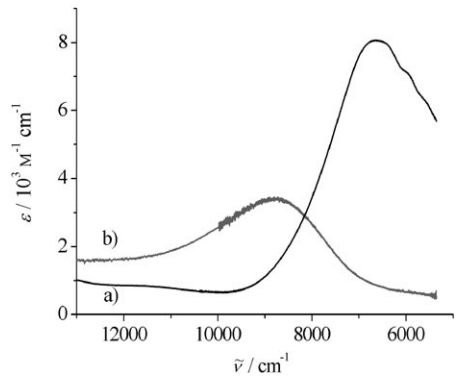

Figure 6. Near-IR spectroelectrochemistry at −25 °C and at applied potentials from 0.2 to 0.4 V ($v = 5\ mV\,s^{-1}$) with 0.1 mol dm^{-3} $NBu_4B(C_6F_5)_4$: a) 1:1 mixture of 5.0×10^{-3} mol dm^{-3} *anti*-**FeRh(cod)** and *syn*-**FeRh(cod)**; b) *anti*-**$FeRh(CO)_2$** and *syn*-**$FeRh(CO)_2$**.

The values of $\tilde{\nu}_{max}$ and $\Delta\tilde{\nu}_{1/2}$ in THF/n-Bu_4NBF_4[9e] previously obtained for *anti*-**FeRh(cod)$^+$** are quite similar. Hence, the band of Figure 6a could be due to the IT transition of the *anti* cation or most likely to the sum of two similar absorptions of isomeric *anti* and *syn* cations, as suggested by the reactivity upon oxidation of the same mixture. The experimental bandwidth of $(\Delta\tilde{\nu}_{1/2})_{obsd} = 1960\ cm^{-1}$ is much lower than the theoretical value ($3620\ cm^{-1}$) expected for a trapped mixed-valent (Class II) redox-asymmetric complex, and the related magnitude of Γ is 0.46 (Table 4). Furthermore, as previously reported,[9e] no dependence of $\tilde{\nu}_{max}$ on solvent or ionic strength was observed. These results indicate that *syn*-**FeRh(cod)$^+$** and *anti*-**FeRh(cod)$^+$**, in analogy to *syn*-**Rh_2^+**, can be classified as borderline Class II/III mixed-valent species.

In Figure 6b the near-IR spectrum of the mixture of *syn*-**$FeRh(CO)_2^+$** and *anti*-**$FeRh(CO)_2^+$** is shown. By replacing the olefin ligands with carbon monoxide the IT band is strongly blue-shifted of $1200\ cm^{-1}$, as expected on basis of the electron-withdrawing properties of CO.

DFT studies: A DFT computational study was carried out to investigate the geometric and electronic structure of the neutral title compounds and of their mixed-valent ions. The discussion of the results starts from the diiron isomers and is followed by the dirhodium isomers and finally the heterobimetallic iron/rhodium species.

The crystallographic geometry of *anti*-[{Fe(Cp)}$_2$(μ-η^5:η^5-*as*-indacenediide)] was fully optimised at the B3LYP level of theory (see Experimental Section). The calculation converged to the C_2-symmetric structure of *anti*-**Fe_2**.[21] The most significant interatomic distances and angles are reported in Table 5, together with the corresponding experimental values. In *anti*-**Fe_2** the *as*-indacenediide bridge is planar and the slippage parameters of the metal centres and the folding angles of the Cp rings are almost zero,[22] as expected for iron metallocenes.[23] The distances between the iron atoms and the centroids of the Cp rings, which are arranged in an eclipsed conformation, compare nicely with those of biferrocene[24] (Table 5).

A full geometry optimisation at the same level of theory was carried out on a model complex for *syn*-[{Fe(Cp)}$_2$(μ-η^5:η^5-*as*-indacenediide)] (*syn*-**Fe_2**), for which crystallographic data are not available yet (Table 5). In the structure of *syn*-**Fe_2** strong bending of the *as*-indacenediide bridge is predicted, accompanied by significant slippage of the metal groups and moderate Cp folding angles. In addition, the FeCp groups are disposed in a staggered conformation. All these features are imposed by the steric congestion of the adjacent FeCp units.

The HOMOs of *anti*-**Fe_2** and *syn*-**Fe_2** exhibit similar lobes: they are both formed by Fe d_{xy} and $d_{x^2-y^2}$ orbitals combined in bonding fashion with HOMO−1 ("b" symmetry according to C_2 labelling) of *as*-indacenediide. The LUMOs of both compounds are formed by the LUMO of the hydrocarbon bridge ("a" symmetry according to C_2 labelling) combined with Fe d_{xz} and d_{yz} orbitals. The largest contribution of Fe d_{z^2} is found in HOMO−6. On the basis of the HOMO–LUMO gaps, which are 4.30 (*anti*-**Fe_2**) and 4.34 eV (*syn*-**Fe_2**), there is no appreciable difference in the stability of these two isomers at the level of theory employed.

Unrestricted B3LYP geometry optimisations on the mono-oxidised species converged to the *anti*-**Fe_2^+** and *syn*-**Fe_2^+** isomers. The full geometry optimisation of the *anti* cation initially converged to a C_2-symmetric species, which was subsequently found to lie at a higher energy (5.4 kcal mol^{-1}) than the asymmetric C_1 structure calculated by breaking the symmetry (see Experimental Section). Vibrational analysis confirmed that they are both energy minima and correspond to two different doublet electronic states. In the following discussion the asymmetric lower energy state is considered.

In both *anti*-$\mathbf{Fe_2}^+$ and *syn*-$\mathbf{Fe_2}^+$ the structural asymmetry is significant, and remarkable geometric differences between the two iron environments are predicted. The distance between one iron centre and the centroid of its coordinated Cp ring is unchanged upon oxidation. On the contrary, the significant increase in the corresponding distance between the other metal centre and the centroid of its coordinated Cp ring suggests that one Fe centre bears almost the entire positive charge. This breaking of the molecular symmetry upon oxidation has been observed also in the pair of crystallographic structures biferrocene/biferrocenyl ion;[24,25] their relevant structural parameters, which were taken from Cambridge Structural Database,[26] are included in Table 5 for comparison.

The values of the Mulliken spin densities on the metal nuclei of *anti*-$\mathbf{Fe_2}^+$ and *syn*-$\mathbf{Fe_2}^+$ are consistent with two homobimetallic cations in which the odd electron is mainly localised on a single metal centre (Table 6). Concomitant with

Table 6. Mulliken spin densities on the metal nuclei.

	syn-$\mathbf{Fe_2}^+$	*anti*-$\mathbf{Fe_2}^+$
Fe1	−0.041	−0.042 [0.63][a]
Fe2	1.40	1.38 [0.63][a]
	syn-$\mathbf{H\text{-}Rh_2}^+$	*anti*-$\mathbf{H\text{-}Rh_2}^+$
Rh1	0.21	0.17
Rh2	0.16	0.17
	syn-**FeRh(cod)**$^+$	*anti*-**FeRh(cod)**$^+$
Fe	0.001	0.003
Rh	1.32	1.29

[a] Mulliken spin densities on the calculated C_2-symmetric higher energy geometry.

spin localisation, appreciable charge separation is also calculated for both complexes, that is, $\Delta q = 0.10$. Pictures of the Kohn–Sham HOMOs of both *anti*-$\mathbf{Fe_2}^+$ and *syn*-$\mathbf{Fe_2}^+$ clearly show that the odd electron is localised to a large extent on one of the Fe atoms (Figure 7).

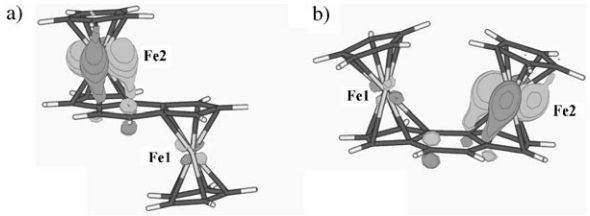

Figure 7. Highest occupied Kohn–Sham spin orbitals (91α) of *anti*-$\mathbf{Fe_2}^+$ (a) and *syn*-$\mathbf{Fe_2}^+$ (b). The density is 0.05 $(ea_0^{-3})^{1/2}$.

The geometric and electronic structures of *anti*-$\mathbf{Fe_2}^+$ and *syn*-$\mathbf{Fe_2}^+$ indicate that these ions are partially trapped mixed-valent species. This result is in agreement not only with our experimental findings, but also with the ESR and Mössbauer measurements reported by Manriquez and coworkers on *anti*-[{Fe(Cp*)}$_2$(μ-η^5:η^5-*as*-indacenediide)]$^+$.[9g]

The model complexes *anti*-$\mathbf{H\text{-}Rh_2}$ and *syn*-$\mathbf{H\text{-}Rh_2}$ were fully optimised at the same level of theory, that is, B3LYP/SDD,6-31G(d,p) (see Experimental Section), starting from the crystallographic structures of *anti*-$\mathbf{Rh_2}$ and *syn*-$\mathbf{Rh_2}$[9f,27] and replacing the methyl substituents with H atoms. The symmetry of *anti*-$\mathbf{H\text{-}Rh_2}$ is C_2, whereas *syn*-$\mathbf{H\text{-}Rh_2}$ is strongly bent, as observed in the crystallographic structure of the analogous compound. Some interatomic distances and angles are reported in Table 5 and are in good agreement with the experimental structural data. The metal slippage is more pronounced in the rhodium isomers than in the iron isomers. This is related to the number of d electrons of the metal. In fact, in rhodium derivatives a metal–ligand antibonding molecular orbital is occupied (HOMO), and the slippage occurs to relieve this destabilising interaction.[28]

The frontier Kohn–Sham MOs of *anti*-$\mathbf{H\text{-}Rh_2}$ and *syn*-$\mathbf{H\text{-}Rh_2}$ have a significant ligand contribution. Mixing of all five Rh d orbitals occurs and the resulting metal contribution combines in an antibonding fashion with the HOMO−1 ("a" symmetry according to C_2 labelling) of *as*-indacenediide and the LUMO of the hydrocarbon bridge to form the HOMOs and the LUMOs of *anti*-$\mathbf{H\text{-}Rh_2}$ and *syn*-$\mathbf{H\text{-}Rh_2}$, respectively. On the basis of the HOMO-LUMO gap *anti*-$\mathbf{H\text{-}Rh_2}$ is more stable than *syn*-$\mathbf{H\text{-}Rh_2}$; the energy difference is 4.03 and 3.85 eV, respectively.

Unrestricted full geometry optimisations were carried out starting from the geometry of the neutral complexes to obtain the dirhodium cations *anti*-$\mathbf{H\text{-}Rh_2}^+$ and *syn*-$\mathbf{H\text{-}Rh_2}^+$. Salient structural parameters are reported in Table 5. In this case *anti*-$\mathbf{H\text{-}Rh_2}^+$ maintains the C_2 symmetry of the neutral precursor and any attempt to obtain an asymmetric species, as found for *anti*-$\mathbf{Fe_2}^+$, failed at this level of theory. This result is in agreement with the experimental evidence that in *anti*-$\mathbf{Rh_2}^+$ metal–metal communication is more efficient than in *anti*-$\mathbf{Fe_2}^+$. Upon oxidation, the most relevant structural changes involve the metal nuclei: in both *anti* and *syn* isomers a decrease in the distance between rhodium and the centroid of the coordinated Cp moiety is predicted (0.03 Å), accompanied by an increase in the distance between rhodium and the ancillary cod ligands (0.05 Å). No rearrangement of the frontier MOs occurs: both in *anti*-$\mathbf{H\text{-}Rh_2}^+$ and in *syn*-$\mathbf{H\text{-}Rh_2}^+$ the spin orbitals 117α and 117β, which are respectively the highest occupied and lowest unoccupied levels, have qualitatively the same spatial part as the HOMO of the neutral precursors. The spin density is prominently localised on the metal nuclei, and is symmetrically distributed in *anti*-$\mathbf{H\text{-}Rh_2}^+$; in *syn*-$\mathbf{H\text{-}Rh_2}^+$ the Rh1:Rh2 spin density ratio is slightly greater than unity, due to the weak asymmetry of the metal environments (Table 6).

Finally, the heterobimetallic complexes *anti*-**FeRh(cod)** and *syn*-**FeRh(cod)** were fully optimised. The relevant interatomic distances compare nicely with those of the homobimetallic iron and rhodium indacenyl isomers (Table 5); however, interestingly, larger slippage values are predicted in *anti*-**FeRh(cod)**, that is, 0.16 and 0.055, for rhodium and

iron respectively, which compare with values of 0.10 and 0.019 computed for *anti*-**H-Rh$_2$** and *anti*-**Fe$_2$**. The topology of the frontier orbitals in the proximity of the metal centres exhibits the features of both analogous homobimetallic isomers.

The heterobimetallic *syn*-**FeRh(cod)** has the smallest HOMO–LUMO gap among all the investigated neutral indacenyl compounds, that is, 3.70 eV, while the HOMO–LUMO gap of *anti*-**FeRh(cod)** is 3.79 eV.

Upon oxidation, the most important structural changes involve the metal centres. In particular, an appreciable increase in the distances between iron and its coordinated indacenyl Cp moiety and rhodium and its coordinated Cp ring is predicted (Table 5). Inspection of the 104α and 104β spin orbitals, which are respectively the highest occupied and the lowest unoccupied levels, reveals that the former is an antibonding combination of rhodium d orbitals with the π lobes localised on the coordinated Cp moiety, and the latter is composed of iron d orbitals. Notably, the spin density is strongly localised on rhodium in both *syn*-**FeRh(cod)$^+$** and *anti*-**FeRh(cod)$^+$** (Table 6). This result will be stressed in the conclusion.

The trend of the calculated adiabatic ionisation potentials, 5.42 [*syn*-**FeRh(cod)**] = 5.42 [*anti*-**FeRh(cod)**] < 5.59 (*syn*-**Fe$_2$**) = 5.59 (*anti*-**Fe$_2$**) < 5.69 (*syn*-**H-Rh$_2$**) < 5.73 eV (*anti*-**H-Rh$_2$**), indicates that the heterobimetallic complexes are more easily ionised than the diiron and dirhodium compounds and reflects the trend of the $E_{1/2}$ of the voltammetric first wave in nBu$_4$NPF$_6$ (Table 1).

The ten lowest excitation energies were computed by TD-DFT[29] calculations for each mixed-valent ion (see Experimental Section).

The interpretation of the TD-DFT results obtained for *anti*-**Fe$_2$$^+$** and *syn*-**Fe$_2$$^+$** is not straightforward. In fact, below 10000 cm^{-1} there are in both cases six excitation energies with zero or low oscillator strength (< 0.005), characterised by numerous contributions from monoelectronic transitions with either metal–metal charge-transfer or metal d–d character. This precludes a precise assignment, but allows some confidence in the assignment of the near-IR absorptions of *anti*-**Fe$_2$$^+$** and *syn*-**Fe$_2$$^+$** at least in part to metal-to-metal charge-transfer (MMCT) processes.

The lowest absorptions predicted for *anti*-**H-Rh$_2$$^+$** and *syn*-**H-Rh$_2$$^+$** are 8119 and 8932 cm^{-1}, respectively; both have nearly the same oscillator strength (ca. 0.04). Inspection of the pairs of MOs involved in the dominant monoelectronic transitions, that is, HOMOβ–LUMOβ and (HOMO−1)β–LUMOβ, reveals no appreciable MMCT character between the metal centres, as reported recently for other organometallic homobinuclear systems.[3k,19d,30] These absorptions are better interpreted as allowed electronic transitions between filled and empty delocalised frontier levels (Figure 8a).

Finally, for the pair of heterobimetallic cations *anti*-**FeRh(cod)$^+$** and *syn*-**FeRh(cod)$^+$** the lowest excitation energies determined theoretically are almost coincident, that is, 10610 cm^{-1} and 10593 cm^{-1}, in agreement with the observation of a single band in the near-IR spectrum of the mixture.

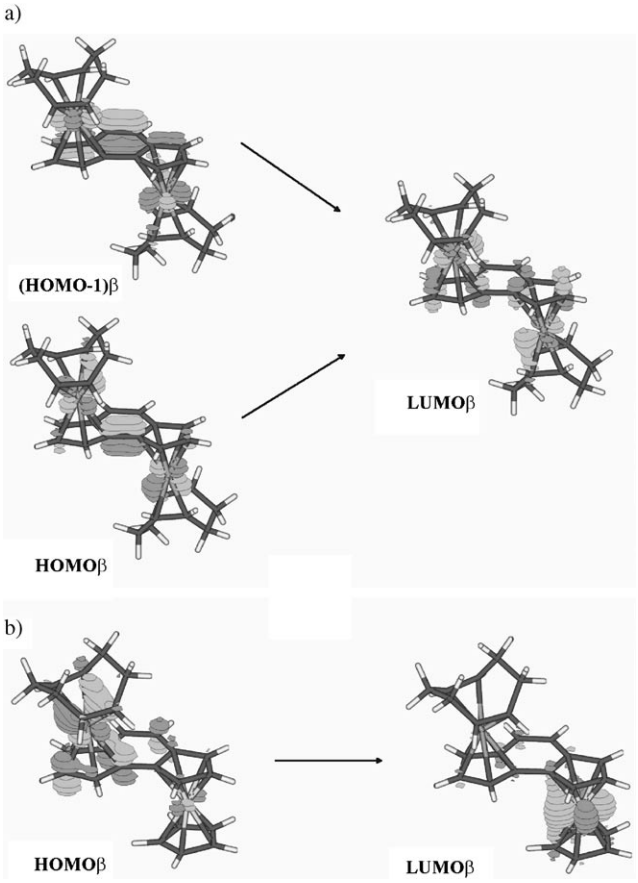

Figure 8. Pairs of Kohn–Sham MOs involved in the lowest absorption for a) *anti*-**H-Rh$_2$$^+$** (HOMO−1)β–LUMOβ and HOMOβ–LUMOβ; b) *anti*-**FeRh(cod)$^+$** HOMOβ–LUMOβ. The density is 0.05 (ea_0^{-3})$^{1/2}$.

The oscillator strengths are 0.02 and 0.004, respectively. These absorptions are an almost pure HOMOβ–LUMOβ transition (*anti*-**FeRh(cod)$^+$**) and a combination of HOMOβ–LUMOβ and HOMOα–LUMOα transitions (*syn*-**FeRh(cod)$^+$**) and are easily assigned to MMCT processes (Figure 8b).

Conclusion

The electrochemical and optical data of homobimetallic diiron mixed-valent cations show that the metal centres in the *anti* and *syn* conformations are rather similarly coupled and belong to Class II. Hence, despite the closer proximity of the two metal atoms in the *syn* isomer, metal-to-metal electronic communication occurs principally through the indacenyl bridge rather than through space. Interestingly, the dinuclear Rh^{I}–Rh^{II} mixed-valent cations show a huge increase in metal-metal interaction relative to their Fe^{II}–Fe^{III} analogues. Moreover, *syn*/*anti* isomerism of the Rh(cod) groups drives the borderline-to-Class III transition.

Even in the heterobimetallic *anti* and *syn* iron–rhodium cations the interaction was found to be much stronger than in the related Fe^{II}–Fe^{III} systems, contrary to the expectation

that, within the Class II limit, redox asymmetry decreases the electronic coupling. They can be classified as borderline systems.

The DFT results reveal that this increased metal–metal interaction in the rhodium indacenyl mixed-valent ions with respect to the analogous iron compounds is related to the metal-ligand bonding mode. The removal of one electron from the HOMO of *anti*-**Fe_2** and *syn*-**Fe_2** complexes generates a trapped ion, because oxidation is a destabilising process due to the metal–ligand bonding character of the highest occupied level. In contrast, the removal of one electron from the HOMO of *anti*-**Rh_2** and *syn*-**Rh_2** leads to the formation of a delocalised ion, because oxidation is a stabilising process due to the metal–ligand antibonding character of the highest occupied level. Finally, oxidation of *anti*-**FeRh(cod)** and *syn*-**FeRh(cod)** occurs at iron, but the odd electron in the cation occupies a rhodium-centred MO. In the hybrid topology of the HOMOs of *anti*-**FeRh(cod)** and *syn*-**FeRh(cod)**, which can be seen as the combination of halves of the corresponding diiron and dirhodium homobimetallic compounds, both iron–ligand bonding and rhodium–ligand antibonding contributions are present. After oxidation we find these contributions in the rhodium-centred HOMO and in the iron-centred LUMO, respectively. As a consequence, high reactivity of rhodium in the heterobimetallic mixed-valent ion is expected.

In fact, substitution of cod with CO in [FeCp(μ-η^5:η^5-*as*-indacenediide)Rh(cod)]$^+$ takes place much more easily than in the corresponding neutral compound. Moreover, the characteristics of the rhodium-to-iron MMCT absorption observed in the near-IR indicate the presence of strong metal–metal electronic coupling in the cationic species. In conclusion, the first oxidation occurs at the iron centre, with concomitant electron transfer from rhodium to iron to give rise to a formally 17-electron rhodium site which is coordinatively unsaturated, highly reactive towards entering CO and susceptible to rapid and efficient ligand exchange.

In summary, thanks to the availability of diiron, dirhodium and iron–rhodium stereoisomers, this joint experimental and computational study reveals that electronic coupling varies in the order *anti*-**Rh_2^+** > *syn*-**Rh_2^+** ≥ *anti*-**FeRh(cod)$^+$** ≈ *syn*-**FeRh(cod)$^+$** ≫ *anti*-**Fe_2^+** > *syn*-**Fe_2^+**.

Experimental Section

All reactions and manipulations of complexes were performed in an oxygen- and moisture-free atmosphere using standard Schlenk techniques or in a Mecaplex glove box. Solvents were dried by refluxing over the appropriate drying agent and distilled under stream of argon. The following compounds were prepared according to the published procedures: [CpFe(C$_5$H$_4$COMe)]BF$_4$,[31] 1,6-, 1,8- and 3,6-*as*-dihydroindacene,[32] *anti*-**Rh_2**,[9f] *syn*-**Rh_2**,[9f] *anti*- and *syn*-[FeCp(μ-η^5:η^5-*as*-indacenediide)Rh(nbd)] (nbd = norbornadiene).[9e] Crystals suitable for X-ray analysis were grown from *n*-pentane solutions at −50 °C.

Synthesis of tetrabutylammonium tetrakis(pentafluorophenyl)borate: The synthesis of lithium tetrakis(pentafluorophenyl)borate was previously reported.[33a] Here, a modified and more detailed procedure[33b] is presented. Bromopentafluorobenzene (5.6 mL, 44.92 mmol) was dissolved under argon in dry pentane (150 mL) placed in a three necked flask equipped with two pressure-equalised dropping funnels and a stirrer bar. The reaction mixture was then de-aerated by bubbling with argon and cooled to −78 °C. A solution of *n*BuLi in hexanes (28 mL, 44.8 mmol, 1.6 mol dm^{-3}) was transferred by cannula through a rubber septum to the graduated dropping funnel and added dropwise to the reaction vessel. Vigorous stirring was maintained throughout the reaction and the resulting suspension of lithium pentafluorophenyl was stirred for a further ten minutes. A solution of boron trichloride in hexanes (11.23 mL, 11.23 mmol, 1 mol dm^{-3}) was transferred by cannula through a rubber septum to the graduated dropping funnel and added dropwise over fifteen minutes to the reaction vessel. The reaction mixture was stirred for forty minutes and then allowed slowly to warm to 25 °C. **Warning:** Care must be taken in handling boron trichloride, which can react explosively and moreover, an excess of lithium pentafluorophenyl could decompose explosively if the reaction vessel warms too quickly. Once at room temperature, the reaction mixture was filtered to yield a white powder. This solid was extracted with dichloromethane (150 mL), and the solution filtered and evaporated to yield a pale yellow gummy solid. The crude product was triturated with hexane, and a white precipitate formed on adding a small amount of dichloromethane. Supernatant liquid was removed by cannula and the lithium tetrakis(pentafluorophenyl)borate was isolated as a white air-stable powder.

Tetrabutylammonium tetrakis(pentafluorophenyl)borate was prepared by metathesis of lithium tetrakis(pentafluorophenyl)borate with tetrabutylammonium chloride, as previously described,[35] and recrystallised from dichloromethane/diethyl ether (1/1). Yield 28 %; m.p. 136–138 °C; elemental analysis calcd (%) for $C_{40}H_{36}F_{20}BN$ (921.57): C 52.13, H 3.94, N 1.52; found: C 52.40, H 3.99, N 1.51; ^{1}H NMR (400.13 MHz, $CDCl_3$, 25 °C, TMS): δ = 3.01 (m, 2H, Hα), 1.54 (m, 2H, Hβ), 1.33 (sextet, 2H, ^3J(Hβ,Hγ) = ^3J(Hγ,Hδ) = 7.4 Hz, Hγ), 0.94 ppm (t, 3H, ^3J(Hγ,Hδ) = 7.4 Hz, Hδ); ^{19}F NMR (376.44 MHz, $CDCl_3$, 25 °C, CCl_3F), δ = −136.50 (m, 2F, F2, F6), −167.82 (t, 1F, ^3J(F3,F4) = ^3J(F4,F5) = 20.3 Hz, F4), −171.75 ppm (m, 2F, F3,5).

Synthesis of *anti*-Fe_2 and *syn*-Fe_2: Method A: A mixture of 1,6-, 1,8- and 3,6-*as*-dihydroindacene (200 mg, 1.3 mmol) was dissolved in distilled THF (35 mL) under argon. *t*BuLi in pentane (1.7 μL, 2.9 mmol, 1.7 mol dm^{-3}) was added dropwise by syringe to the stirred and cooled (−50 °C) solution. The mixture was stirred for 1 h and the temperature raised to −5 °C. After cooling the solution to −78 °C solid [Fe(CO)$_2$(Cp)I] (788 mg, 2.594 mmol) was added. After 2 h the solvent was evaporated to yield a dark orange solid. IR (methylcyclohexane): $\tilde{\nu}$ = 2003 (s), 1961 (s), 1952 cm^{-1}(s) (C≡O); NMR: The ^{1}H NMR spectrum of the [{Fe(CO)$_2$(Cp)}$_2$(μ-η^1:η^1-*as*-indacenediide)] species showed the existence of several isomers, but a detailed study with 2D NMR measurements was hampered by decomposition that occurs in different deuterated solvents (C_6D_6, $(CD_3)_2CO$, CD_2Cl_2). The crude product was extracted with several portions of ice-cold methylcyclohexane, and the fractions were collected in the photolysis cell. During photolysis argon was bubbled into the solution and the solution stirred. The reaction was monitored by IR until disappearance of the CO bands. The red-violet product (59 % yield) obtained after solvent evaporation was a 3:1 mixture of *anti*-**Fe_2** and *syn*-**Fe_2**,as indicated by NMR analysis, an isomeric ratio identical to that found by using Method B (see Supporting Information). The crude product was eluted on a neutral Al_2O_3 column with petroleum ether and petroleum ether/diethyl ether (90:10). *syn*-**Fe_2** proved to be less stable than *anti*-**Fe_2**. By using a short column (10 cm) and small quantities of crude mixture, pure *anti*-**Fe_2**, a 1:1.5 fraction enriched in *syn*-**Fe_2** and a 1:1 mixture were obtained. Crystals of *anti*-**Fe_2** suitable for X-ray analysis were grown from diethyl ether/*n*-hexane solution at −30 °C. Elemental analysis calcd (%) for $C_{22}H_{18}Fe_2$: C 67.05, H 4.60; found: C 64.55, H 4.68.

syn-**Fe_2**: ^{1}H NMR (400.13 MHz, [D$_6$]acetone, 25 °C, TMS), δ = 6.98 (s, 2H, H4, H5), 4.80 (dd, 2H, ^3J(H1,H2) = ^3J(H7,H8) = 2.4 Hz, ^4J(H1,H3) = ^4J (H6,H8) = 1.0 Hz H1,H8), 4.57 (dd, 2H, ^3J(H2,H3) = ^3J(H6,H7) = 2.4 Hz, ^4J(H1,H3) = ^4J(H6,H8) = 1.0 Hz H3, H6), 4.25 (s, 5H, Cp), 4.10 ppm (t, 2H, ^3J(H1,H2) = ^3J(H2,H3) = 2.4 Hz H2, H7); ^{13}C{^{1}H} NMR (100.61 MHz, [D$_6$]acetone, 25 °C, TMS) δ = 125.40 (C4, C5), 89.41 (C3a, C6a), 83.60 (C1a, C8a), 69.45 (Cp), 67.42 (C2, C7), 64.50 (C1, C8),

64.33 ppm (C3, C6). *anti*-**Fe_2**: ^{1}H NMR (400.13 MHz, [D$_6$]acetone, 25 °C, TMS): $\delta = 6.91$ (s, 2H, H4, H5), 4.89 (dd, 2H, ^3J(H1,H2) = ^3J(H7,H8) = 2.5 Hz, ^4J(H1,H3) = ^4J(H6,H8) = 1.1 Hz, H1, H8), 4.59 (dd, 2H, ^3J(H2,H3) = ^3J(H6,H7) = 2.5 Hz, ^4J(H1,H3) = ^4J(H6,H8) = 1.1 Hz, H3, H6), 4.12 (t, 2H, ^3J(H1,H2) = ^3J(H2,H3) = 2.4 Hz H2, H7), 3.68 ppm (s, 5H, Cp); ^{13}C{^{1}H} NMR (100.61 MHz, [D$_6$]acetone, 25 °C, TMS): $\delta = 125.22$ (C4, C5), 84.51 (C3a, C6a), 83.03 (C1a, C8a), 70.15 (Cp), 68.07 (C2, C7), 65.98 (C3, C6), 62.33 ppm (C1, C8). ESI-MS: *m/z*: 394 [M^+], 329 [M^+ −Cp].

Synthesis of *anti*-FeRh(cod) and *syn*-FeRh(cod): The previously reported synthesis[9e] was modified in part. Monometallic [FeCp(η^5-1-hydro-*as*-indacenyl)] and [FeCp(η^5-3-hydro-*as*-indacenyl)] were prepared according to the thermophotochemical procedure reported for the diiron complexes (Method B). The conditions for Rh(cod) coordination to the second indacenyl Cp ring are identical to those already described. A 1:1 mixture of *anti*-**FeRh(cod)** and *syn*-**FeRh(cod)** was obtained. Yield 82%. ^{1}H NMR and ^{13}C{^{1}H} NMR data corresponded to those already reported.

Synthesis of *anti*-FeRh(CO)$_2$ and *syn*-FeRh(CO)$_2$: The reaction was performed in a stainless steel autoclave provided with a mechanical stirrer and temperature control (±0.5 °C). Carbon monoxide was supplied from a gas reservoir connected to the autoclave through a constant-pressure regulator. A solution of a 1:3 mixture of *anti*-**FeRh(nbd)** and *syn*-**FeRh(nbd)** (30 mg, 0.064 mmol) in distilled THF (25 mL) was poured into a Pyrex beaker, which was placed in the autoclave. The reaction conditions were $T = 50$ °C, $P = 11$ atm, $t = 6$ h. The solvent was evaporated and the residue washed with degassed cyclohexane (25 mL) to give a 1:3 mixture of *syn* and *anti* isomers as a dark red solid. Yield: 80%. Elemental analysis calcd (%) for $C_{21}H_{13}FeRhO_2$: C 55.30, H 2.87. Found: C 58.01, H 2.88. IR (CH_2Cl_2): $\tilde{\nu} = 2037$ (s), 1974 cm^{-1} (s).

syn-**FeRh(CO)$_2$**: ^{1}H NMR (400.13 MHz, [D$_6$]acetone, 25 °C, TMS), $\delta =$ 7.35 and 6.98 (2H, AB quartet, $J_{A,B} = 9.2$ Hz, H4 and H5 respectively), 6.17 (ddd, 1H, ^3J(H7,H8) = 2.8, ^4J(H6,H8) = 1.8, ^{5}J(H5,H8) = 0.8 Hz, H8), 5.94 (dt, 1H, ^3J(H6,H7) = ^3J(H7,H8) = 3.0, J(^{103}Rh,H7) = 1.9 Hz, H7), 5.79 (m, 1H, H6), 5.15 (m, 1H, H1), 4.80 (dd, 1H, ^3J(H2,H3) = 2.6, ^4J(H1,H3) = 1.1 Hz, H3), 4.18 (t, 1H, ^3J(H1,H2) = ^3J(H2,H3) = 2.6 Hz, H2), 3.90 ppm (s, 5H, Cp); ^{13}C{^{1}H} NMR (100.61 MHz, [D$_6$]acetone, 25 °C, TMS): $\delta = 128.70$ (C4), 117.47 (C5), 92.44 (C7), 79.32 (C6), 78.67(C8), 72.20 (Cp), 69.98 (C2), 63.77 (C3), 61.73 ppm (C1). *anti*-**FeRh(CO)$_2$**: ^{1}H NMR (400.13 MHz, [D$_6$]acetone, 25 °C, TMS), $\delta = 7.18$ and 6.98 (2H, AB quartet, $J_{A,B} = 9.2$ Hz, H4 and H5, respectively) 6.23 (ddd, 1H, ^3J(H7,H8) = 2.9 Hz, ^4J(H6,H8) = 1.7 Hz, ^{5}J(H5,H8) = 0.9 Hz, H8), 5.92 (dt, 1H, ^3J(H6,H7) = ^3J(H7,H8) = 2.9 Hz, J(^{103}Rh,H7) = 1.8 Hz, H7), 5.87 (m, 1H, H3), 5.07 (m, 1H, H1), 4.85 (dd, 1H, ^3J(H2,H3) = 2.5 Hz, ^4J(H1,H3) = 1.1 Hz, H3), 4.16 (t, 1H, ^3J(H1,H2) = ^3J(H2,H3) = 2.5 Hz, H2), 3.76 ppm (s, 5H,Cp); ^{13}C{^{1}H} NMR (100.61 MHz, [D$_6$]acetone, 25 °C, TMS): $\delta = 126.88$ (C5), 91.53 (C7), 80.48 (C6), 78.14 (C8), 69.72 (C6), 69.28 (Cp), 65.28 (C3), 61.73 ppm (C8).

Physical measurements: The X-ray structures were obtained by collecting intensity data at room temperature on a Philips PW1100 single-crystal diffractometer (FEBO system) with graphite-monochromated $Mo_{K\alpha}$ radiation by following standard procedures. All intensities were corrected for Lorentzian polarization and absorption.[34a] The structure was solved by direct methods using SIR-97.[34b] Refinement was carried out by full-matrix least-squares procedures on F_o^2 with anisotropic temperature factors for all non-hydrogen atoms. The H atoms were placed in calculated positions with fixed, isotropic thermal parameters (1.2 U_{equiv} of the parent carbon atom). The calculations were performed with the SHELXL-97 program[34c] implemented in the WinGX package.[34d]

ESI-MS spectra were recorded with a MSD SL Trap mass spectrometer (Agilent Technologies, Palo Alto, CA, USA) operating in positive-ion mode from *m/z* 100 to 2200. A 5×10^{-6} mol dm^{-3} solution in CH_2Cl_2 was directly infused into the ion source at a flow rate of 10^{-6} dm^3 min^{-1} by a syringe pump. The capillary voltage was set at 3500 V, the nebuliser pressure at 100 psi, the dry gas at 3 dm^3 min^{-1} and 300 °C, the capillary exit at 145 V, and the skimmer at 40 V.

IR spectra were recorded on a Bruker Equinox 55 FT-IR spectrometer. ^{1}H and ^{13}C NMR spectra were obtained on a Bruker Avance DRX spectrometer ($T = 298$ K) operating at 400.13 and 100.61 MHz, respectively. The proton resonances were assigned by standard chemical shift correlation and NOESY experiments. The ^{13}C resonances were assigned through 2D heterocorrelated COSY experiments (HMQC[36a] with pulsed field gradients for coherence and quadrature detection in F1 achieved by using the TPPI method[36b–d] for the H-bonded C atoms, and HMBC[36e–f] for the quaternary C atoms). All ^{103}Rh NMR spectra (CD_2Cl_2, $T = 300$ K) were acquired on a Bruker Avance DRX spectrometer with a 5 mm inverse low-frequency probe head and a *z*-gradient coil (90−(^{1}H) = 7.50 μs, 90−(^{103}Rh) = 7 μs). The HMBC experiments were carried out with the sequence already reported.[17] The spectral width for ^{1}H was 10 ppm. For ^{103}Rh the spectral width was initially 3000 ppm, and finally 500 ppm in order to improve resolution. The δ(^{103}Rh) values were calculated by determining the absolute frequency of the cross peak and relating it to the arbitrary reference frequency ($\Xi = 3.16$ MHz at 100.00 MHz). The concentration of the samples was 6×10^{-2} mol dm^{-3}.

CV experiments were performed in an air-tight three-electrode cell connected to a vacuum/argon line. The reference electrode was an SCE (Tacussel ECS C10) separated from the solution by a bridge compartment filled with the same solvent/supporting electrolyte solution used in the cell. The counterelectrode was a platinum spiral with about 1 cm^2 apparent surface area. The working electrodes were disks obtained from cross-sectioning gold wires of different diameters (0.5, 0.125 and 0.025 mm) sealed in glass. Between successive CV scans the working electrodes were polished on alumina according to standard procedures and sonicated before use. An EG&G PAR-175 signal generator was used. The currents and potentials were recorded on a Lecroy 9310L oscilloscope. The potentiostat was home-built with a positive feedback loop for compensation of ohmic drop.[37]

Mid-IR, near-IR and visible spectroelectrochemistry experiments at variable temperatures were carried out with a cryostatically controlled (low-T) Optically Transparent Thin-Layer Electrochemical (OTTLE) cell (IDEAS!UvA B.V., University of Amsterdam, The Netherlands)[38] equipped with CaF_2 windows. Pt working (80% transmittance), Pt auxiliary minigrid electrodes, and pseudoreference Ag wire, melt-sealed in the insulating polyethylene spacer with an optical path of 0.019 cm.

Computational details: All DFT calculations were performed with the software package Gaussian 03.[39] The B3LYP functional was employed, which includes a mixture of Hartree–Fock exchange with DFT exchange correlation given by Becke's three-parameter functional, which includes both local and non-local terms.[40] The choice of this functional was motivated by its successful performance reported in recent studies on electronic coupling in mixed-valent organometallic complexes.[3l,19d,30,41] All-electron 6-31G(d,p) basis sets were used for C and H;[42a,b] Fe was described with Stuttgart relativistic small-core ECP basis set.[42c] This level of theory is abbreviated in the text as B3LYP/SDD,6-31G(d,p). Pictures of the frontier levels of the neutral title compounds are shown in the Supporting Information. The spin contamination was monitored in the calculations on the charged open-shell species (UB3LYP/SDD,6-31G(d,p)), and its value was very close to 0.75, as expected for a doublet state. The stationary nature of the minima was confirmed by running frequency calculations. Full geometry optimisations of the ions were attempted also at the unrestricted Hartree–Fock (UHF) level of theory with the same basis sets as used in DFT calculations (UHF/SDD,6-31G(d,p)), but a significant degree of spin contamination precluded any reliability of the wave function. The molecular symmetry in the geometry optimisations of *anti*-**Fe_2^+** and *anti*-**H-Rh_2^+** was broken, but only in the case of the former cation did the calculation converge to a C_1-symmetric ion. TD-DFT calculations were carried out at the B3LYP/SDD,6-31G(d,p) level of theory both on the neutral complexes and on the mixed valence cations. The inclusion of diffuse functions in C and H basis sets (6-31+G(d,p)) was tested and was found not to significantly modify the results. The lowest ten excitations were calculated and assigned by comparison with the experimental spectra and on the basis of the oscillator strengths. The difference between the theoretical and the experimental energies is within the tolerance accepted for this kind of analysis on large open-shell organometallic molecules.[3l,19d,30,41,43]

Acknowledgements

This work was supported by the Ministero dell'Istruzione, dell'Università e della Ricerca (MIUR) within PRAT 2002, PRIN 2003, and Attrezzature Scientifiche 2003 research projects. CINECA (Consorzio di calcolo del Nord-Est, Casalecchio di Reno) is gratefully acknowledged for the access to the computational facilities, that is, IBM SP5. We gratefully acknowledge Prof. Thomas E. Bitterwolf for his helpful comments and punctual suggestions, and Dr. Ester Marotta for ESI-MS analysis.

[1] a) D. M. D'Alessandro, F. R. Keene, *Chem. Rev.* **2006**, *106*, 2270–2298; b) R. J. Crutchley, *Angew. Chem.* **2005**, *117*, 6610–6612; *Angew. Chem. Int. Ed.* **2005**, *44*, 6452–6454; c) A. Ceccon, S. Santi, L. Orian, A. Bisello, *Coord. Chem. Rev.* **2004**, *248*, 683–724; d) N. Robertson, C. A. McGowan, *Chem. Soc. Rev.* **2003**, *32*, 96–103; e) R. M. Williams, L. De Cola, F. Hartl, J.-J. Lagref, J.-M. Planeix, A. De Cian, M. W. Hosseini, *Coord. Chem. Rev.* **2002**, *230*, 253–261; f) T. E. Bitterwolf, *Coord. Chem. Rev.* **2000**, *206*, 419–450; g) W. Kaim, A. Klein, M. Glöckle, *Acc. Chem. Res.* **2000**, *33*, 755–763; h) N. Wheatley, P. Kalck, *Chem. Rev.* **1999**, *99*, 3379–3420; i) J. Heck, S. Dabek, T. Meyer-Friedrichsen, H. Wong, *Coord. Chem. Rev.* **1999**, *190–192*, 1217–1254; j) P. Belser, S. Bernhard, C. Blum, A. Beyeler, L. De Cola, V. Balzani, *Coord. Chem. Rev.* **1999**, *190–192*, 155–169; k) L. De Cola, P. Belser, *Coord. Chem. Rev.* **1998**, *177*, 301–346; l) F. Paul, C. Lapinte, *Coord. Chem. Rev.* **1998**, *178–180*, 431–509; m) D. Astruc, *Acc. Chem. Res.* **1997**, *30*, 383–391; n) S. Barlow, D. O'Hare, *Chem. Rev.* **1997**, *97*, 637–670; o) M. D. Ward, *Chem. Soc. Rev.* **1995**, *31*, 121–133.

[2] a) C. C. Allen, N. S. Hush, *Prog. Inorg. Chem.* **1967**, *8*, 357–391; b) N. S. Hush, *Prog. Inorg. Chem.* **1967**, *8*, 391-444; c) M. B. Robin, P. Day, *Adv. Inorg. Chem. Radiochem.* **1967**, *10*, 247; d) C. Creutz, *Prog. Inorg. Chem.* **1983**, *30*, 1–73; e) D. E. Richardson, H. Taube, *Coord. Chem. Rev.* **1984**, *60*, 107–129; f) R. J. Crutchley, *Adv. Inorg. Chem.* **1994**, *41*, 273–325; g) P. Chen, T. J. Meyer, *Chem. Rev.* **1998**, *98*, 1439–1477; h) B. S. Brunschwig, N. Sutin, *Coord. Chem. Rev.* **1999**, *187*, 233–254; i) J. P. Launay, *Chem. Soc. Rev.* **2001**, *30*, 386–397; j) K. D. Demadis, C. M. Haertshorn, T. J. Meyer, *Chem. Rev.* **2001**, *101*, 2655–2685; k) B. S. Brunschwig, C. Creutz, N. Sutin, *Chem. Soc. Rev.* **2002**, *31*, 168–184; l) D. M. D'Alessandro, F. R. Keene, *Chem. Soc. Rev.* **2006**, *35*, 424–440.

[3] a) D. M. D'Alessandro, P. H. Dinolfo, J. T. Hupp, P. C. Junk, F. R. Keene, *Eur. J. Inorg. Chem.* **2006**, *4*, 772–783; b) K. Heinze , K. Hempel, M. Beckmann, *Eur. J. Inorg. Chem.* **2006**, *10*, 2040–2050; c) J. C. Salsman, S. Ronco, C. H. Londergan, C. P. Kubiak, *Inorg. Chem.* **2006**, *45*, 547–554; d) S. I. Ghazala, F. Paul, L. Toupet, T. Roisnel, P. Hapiot, C. Lapinte, *J. Am. Chem. Soc.* **2006**, *128*, 2463–2476; e) H. Sun, J. Steeb, A. E. Kaifer, *J. Am. Chem. Soc.* **2006**, *128*, 2820–2821; f) F. A. Cotton, C. A. Murillo, D. Villagrán, R. Yu, *J. Am. Chem. Soc.* **2006**, *128*, 3281–3290; g) T.-Y. Dong, K. Chen, M.-C. Lin, L. Lee, *Organometallics* **2005**, *24*, 4198–4206; h) P. H. Dinolfo, S. J. Lee, V. Coropceanu, J.-L. Brédas, J. T. Hupp, *Inorg. Chem.* **2005**, *44*, 5789–5797; i) G. Laus, C. E. Strasser, M. Holzer, K. Wurst, G. Pürstinger, K.-H. Ongania, M. Rauch, G. Bonn, H. Schottenberger, *Organometallics* **2005**, *24*, 6085–6093; j) A. C. Benniston, A. Harriman P. Li, C. A. Sams, M. D. Ward, *J. Am. Chem. Soc.* **2004**, *126*, 13630–13631; k) M. I. Bruce, K. Costuas, T. Davin, B. G. Ellis, J.-F. Halet, C. Lapinte, P. J. Low, M. E. Smith, B. W. Skelton, L. Toupet, A. H. White, *Organometallics* **2005**, *24*, 3864–3881; l) F. A. Cotton, C. Y Liu, C. A. Murillo, D. Villagrán, X. Wong, *J. Am. Chem. Soc.* **2004**, *126*, 14822–14831; m) S. Welter, K. Brunner, J. W. Hofstraat, L. De Cola, *Nature* **2003**, *421*, 54–57; n) K. M-C. Wong, S. C.-F. Lam, C.-C. Ko, N. Zhu, V. W.-W. Yam, S. Roué, C. Lapinte, S. Fathallah, K. Costuas, S. Kahlal, J.-F. Halet, *Inorg. Chem.* **2003**, *42*, 7086–7098; o) J. Y. Chen, C.-H. Kao, S. J. Lin, C.-C. Tai, K. S. Kwan, *Inorg. Chem.* **2000**, *39*, 189–194.

[4] a) C. G. de-Azevedo, K. P. C. Vollhardt, *Synlett* **2002**, 1019–1042; b) C. G. Atwood, W. E. Geiger, *J. Am. Chem. Soc.* **2000**, *122*, 5477–5485; c) H. Schottenberger, M. Buchmeiser, C. Rieker, P. Jaitner, K. Wurst, *J. Organomet. Chem.* **1997**, *541*, 249–260; d) P. A. McGovern, K. P. C. Vollhardt, *Synlett* **1990**, 493–500; e) M.-H. Desbois, D. Astruc, J. Guillin, J.-P Mariot, F. Varret, *J. Am. Chem. Soc.* **1985**, *107* , 5280–5282; f) N. G. Connelly, A. R. Lucy, J. D. Payne, A. M. R. Galas, W. E. Geiger, *J. Chem. Soc. Dalton Trans.* **1983**, 1879; g) E. W. Neuse, M. S. Loonat, *Transition Met. Chem.* **1981**, *6*, 260–263; h) C. LeVanda, K. Bechgaard, D. O. Cowan, M. D. Rausch, *J. Am. Chem. Soc.* **1977**, *99*, 2964–2968.

[5] a) S. C. Jones, S. Barlow, D. O'Hare, *Chem. Eur. J.* **2005**, *11*, 4473–4481; b) S. Barlow, *Inorg. Chem.* **2001**, *40*, 7047–7053; c) P. Härter, G. Boguth, E. Hedtweck, J. Riede, *Angew. Chem.* **1989**, *101*, 1058–1059; *Angew. Chem. Int. Ed. Engl.* **1989**, *28*, 1008–1009; d) T. E. Bitterwolf, *J. Organomet. Chem.* **1986**, *312*, 197–206; e) W. H. Morrison, S. Krogsrud, D. N. Hendrikson, *Inorg. Chem.* **1973**, *12*, 1998–2004.

[6] a) A.-C. Ribou, J.-P. Launey, M. L. Sachtleben, H. Li, C. W. Spangler, *Inorg. Chem.* **1996**, *35*, 3735–3740; b) L. M. Tolbert, X. Zhao, Y. Ding, L. A. Bottomley, *J. Am. Chem. Soc.* **1995**, *117*, 12891–12892; c) M. Sato, A. Kudo, Y. Kawata, H. Saitoh, *Chem. Commun.* **1996**, 25–26.

[7] a) Z. Yuan, G. Stringer, I. R. Jobe, D. Kreller, K. Scott, L. Koch, N. J. Taylor, T. B. Marder, *J. Organomet. Chem.* **1993**, *452*, 115–120; b) C. LeVanda, K. Bechgaard, D. O. Cowan, *J. Org. Chem.* **1976**, *41*, 2700–2704.

[8] a) E. Bunel, P. Campos, J. Rux, L. Valle, I. Chadwick, M. S. Ana, G. Gonzales, J. M. Manriquez, *Organometallics* **1988**, *7*, 474–476; b) C. Patoux, C. Coudret, J.-P. Launey, C. Joachim, A. Gourdon, *Inorg. Chem.* **1997**, *36*, 5037–5049; c) R. D. A. Hudson, B. M. Foxman, M. Rosenblum, *Organometallics* **2000**, *19*, 469–474; d) C. Elschenbroich, M. Wolf, O. Schieman, K. Harms, O. Burghaus, J. Pebler, *Organometallics* **2002**, *21*, 5810–5819.

[9] a) S. C. Jones, P. Roussel, T. Hascall, D. O'Hare, *Organometallics* **2006**, *25*, 221–229; b) S. C. Jones, D. O'Hare, *Chem. Commun.* **2003**, 2208–2209; c) S. C. Jones, T. Hascall, S. Barlow, D. O'Hare, *J. Am. Chem. Soc.* **2002**, *124*, 11610–11611; d) E. Esponda, C. Adams, F. Burgos, I. Chavez, J. M. Manriquez, F. Delpech, A. Castel, H. Gornitzka, M. Rivière-Baudet, P. Rivière, *J. Organomet. Chem.* **2006**, *691*, 3011–3017; e) S. Santi, A. Ceccon, F. Carli, L. Crociani, A. Bisello, M. Tiso, A. Venzo, *Organometallics* **2002**, *21*, 2679–2686; f) A. Ceccon, A. Bisello, L. Crociani, A. Gambaro, P. Ganis, F. Manoli, S. Santi, A. Venzo, *J. Organomet. Chem.* **2000**, *600*, 94–111; g) J. M. Manriquez, M. D. Ward, W. M. Reiff, J. C. Calabrese, N. L. Jones, P. J. Carroll, E. E. Bunel, J. S. Miller, *J. Am. Chem. Soc.* **1995**, *117*, 6182–6193; h) S. Iijima, I. Motoyama, H. Sano, *Chem. Lett.* **1979**, 1349–1352; i) M. K. Amshumali, I. Chávez, V. Arancibia, F. Burgos O, J. M. Manríquez, E. Molins, A. Roig, *J. Organomet. Chem.* **2005**, *690*, 1340–1349; j) G. Alfonso, I. Chávez, V. Arancibia, J. M. Manríquez, M. T. Garland, A. Roig, E. Molins, R. F. Baggio, *J. Organomet. Chem.* **2001**, *620*, 32–38; k) T. J. Katz, W. Ślusarek, *J. Am. Chem. Soc.* **1979**, *101*, 4259–4267.

[10] a) R. J. Cave, M. D. Newton, *Chem. Phys. Lett.* **1996**, *249*, 15–19; b) M. D. Newton, *Chem. Rev.* **1991**, *91*, 767–792; c) G. U. Bublitz, W. M. Laidlaw, R. G. Denning, S. G. Boxer, *J. Am. Chem. Soc.* **1998**, *120*, 6068–6075; d) C. Creutz, M. D. Newton, N. Sutin, *J. Photochem. Photobiol. A* **1994**, *82*, 47–59; e) J. T. Hupp, Y. Dong, R. L. Blackburn, H. Lu, *J. Phys. Chem.* **1993**, *97*, 3278–3282.

[11] a) P. Roussel, M. J. Drewitt, D. R. Cary, C. G. Webster, D. O'Hare, *Chem. Commun.* **1998**, 2205–2206; b) C. Bonifaci, A. Ceccon, A. Gambaro, P. Ganis, S. Santi, A. Venzo, *Organometallics* **1995**, *14*, 2430–2434.

[12] a) H. Atzkern, B. Huber, F. H. Köhler, G. Müller, R. Müller, *Organometallics* **1991**, *10*, 238–244; b) M. Fritz, J. Hiermeier, N. Hertkom, F. H. Köhler, G. Müller, G. Reber, O. Steigelmann, *Chem. Ber.* **1991**, *124*, 1531–1539.

[13] a) M. Stradiotto, D. W. Hughes, A. D. Bain, M. A. Brook, M. J. McGlinchey, *Organometallics* **1997**, *16*, 5563–5568; b) R. C. Kerber, R. Garcia, A. L. Nobre, *Organometallics* **1996**, *15*, 5563–5568; c) J. A. Belmont, M. S. Wrighton, *Organometallics* **1986**, *5*, 1421–

1428; d) R. H. Mitchell, Y. Chen, N. Khalifa, P. Zhou, *J. Am. Chem. Soc.* **1998**, *120*, 1785–1794.

[14] Obtaining hydro-*as*-indacenyl anion from *as*-dihydroindacene is not a trivial problem. An equilibrium among monoanion, dianion and the olefin is established depending on the reaction conditions. This topic is presently under investigation.

[15] The corresponding cationic species were not detected, and neither decomposition nor paramagnetic line broadening and shift were monitored in the ^{1}H NMR spectrum of the reaction mixture (see Supporting Information).

[16] a) K. A. Pevear, M. M. Banaszak, G. B. Carpenter, A. L. Rieger, P. H. Rieger, D. A. Sweigart, *Organometallics* **1995**, *14*, 512–523; b) C. C. Neto, S. Kim, Q. Men, D. A. Sweigart, Y. K. Chung, *J. Am. Chem. Soc.* **1993**, *115*, 2077–2078.

[17] L. Orian, A. Bisello, S. Santi, A. Ceccon, G. Saielli, *Chem. Eur. J.* **2004**, *10*, 4029–4040.

[18] S. F. Nelsen, *Chem. Eur. J.* **2000**, *6*, 581–588.

[19] a) F. Barriére, W. E. Geiger, *J. Am. Chem. Soc.* **2006**, *128*, 3980–3989; b) F. Barriére, N. Camire, W. E. Geiger, U. T. Mueller-Westerhoff, R. Sanders, *J. Am. Chem. Soc.* **2002**, *124*, 7262–7263; c) D. M. D'Alessandro, F. R. Keene, *Dalton Trans.* **2004**, 3950–3954; d) S. Santi, L. Orian, C. Durante, A. Bisello, F. Benetollo, L. Crociani, P. Ganis, A. Ceccon, *Chem. Eur. J.* **2007**, *13*, 1955–1968.

[20] J.-L. M. Abboud, R. Rotario, *Pure Appl. Chem.* **1999**, *71*, 645–718.

[21] EHMO calculations on the indacenyl ligands and diiron indacenyl complexes have been previously reported: M. T. Garland, J. Y. Saillard, I. Chavez, B. Oelckers, J. M. Manriquez, *J. Mol. Struct.* **1997**, *390*, 199–208.

[22] The slippage parameter Δ is defined as $\Delta = 1/2[(M{-}C1a{+}M{-}C3a){-}(M{-}C1{+}M{-}C3)]$; the folding angle FA is the dihedral angle between the planes C1,C2,C3 and C1,C3,C3a,C1a (referring to the numbering scheme of Scheme 1). T. B. Marder, J. C. Calabrese, D. C. Roe, T. H. Tulip, *Organometallics* **1987**, *6*, 2012–2014.

[23] S. A. Westcott, A. K. Kakkar, G. Stringer, N. J. Taylor, T. B. Marder, *J. Organomet. Chem.* **1990**, *394*, 777–794.

[24] A. C. Macdonald, J. Trotter, *Acta Crystallogr.* **1964**, *17*, 872–887.

[25] M.-H. Delville, F. Robert, P. Gouzerh, J. Linares, K. Boukheddaden, F. Varret, D. Astruc, *J. Organomet. Chem.* **1993**, *451*, C10-C12.

[26] J. van de Streek, *Acta Crystallogr. Sect. B* **2006**, *62*, 567–579.

[27] a) P. Ganis, A. Ceccon, T. Kohler, F. Manoli, S. Santi, A. Venzo, *Inorg. Chem. Commun.* **1988**,*1*, 15–18; b) C. Bonifaci, A. Ceccon, A. Gambaro, F. Manoli, L. Mantovani, P. Ganis, S. Santi, A. Venzo, *J. Organomet. Chem.* **1998**, *557(1)*, 97–109; c) L. Orian, P. Ganis, S. Santi, A. Ceccon, *J. Organomet. Chem.* **2005**, *690*, 482–492.

[28] a) T. A. Albright, J. K. Burdett, M.-H. Whangbo, *Orbital Interactions in Chemistry*, Wiley, New York, 1985; b) M. J. Calhorda, L. F. Veiros, *Coord. Chem. Rev.* **1999**, *185–186*, 37–51.

[29] M. E. Casida, C. Jamorski, K. C. Casida, D. R. Salahub, *J. Chem. Phys.* **1998**, *108*, 4439–4449.

[30] L. Medei, L. Orian, O. V. Semeikin, M. G. Peterleitner, N. A. Ustynyuk, S. Santi, C. Durante, A. Ricci, C. Lo Sterzo, *Eur. J. Inorg. Chem.* **2006**, 13, 2582–2597.

[31] N. G. Connelly, W. E. Geiger, *Chem. Rev.* **1996**, *96*, 877–910.

[32] a) I. Erden, F. P. Xu, A. Sadoun, W. Smith, G. Sheff, M. Ossun, *J. Org. Chem.* **1995**, *60*, 813–820; b) T. J. Katz, V. Balogh, J. M. Schulman, *J. Am. Chem. Soc.* **1968**, *90*, 734–739; c) F. Carli, T. di Laurea, University of Padova, Italy, **1999/2000**.

[33] a) A. G. Massey, A. J. Park, F. G. A. Stone, *Proc. Chem. Soc.* **1963**, 212–213; b) A. R. Brown, Edinburgh, personal communication.

[34] a) A. T. C. North, D. C. Philips, F. S. Mathews, *Acta Crystallogr. Sect. A* **1968**, *24*, 351–359; b) SIR-97: A. Altomare, M. C. Burla, M. Camalli, G. L. Cascarano, C. Giacovazzo, A. Guagliardi, A. G. G. Moliterni, G. Polidori, R. Spagna, *J. Appl. Crystallogr.* **1999**, *32*, 115–119; c) G. M. Sheldrick, SHELXL-97, Program for the Refinement of Crystal Structures, University of Göttingen, Germany, **1997**; d) L. J. Farrugia, *J. Appl. Crystallogr.* **1999**, *32*, 837–838.

[35] R. J. LeSuer, W. E. Geiger, *Angew. Chem.* **2000**, *112*, 254–256; *Angew. Chem. Int. Ed.* **2000**, *39*, 248–250.

[36] a) A. Bax, S. Subramanian, *J. Magn. Reson.* **1986**, *67*, 565–569; b) T. Parella, *Magn. Reson. Chem.* **1998**, *36*, 467–495; c) G. W. Vuister, J. Ruiz-Cabello, P. C. M. van Zijl, *J. Magn. Reson.* **1992**, *100*, 282–302; d) W. Willker, D. Leibfritz, R. Kerrsebaum, W. Bermel, *Magn. Reson. Chem.* **1993**, *31*, 287–292; e) A. Bax, M. F. Summers, *J. Am. Chem. Soc.* **1986**, *108*, 2093–2094; f) M. F. Summers, L. G. Marzilli, A. Bax, *J. Am. Chem. Soc.* **1986**, *108*, 4285–4294.

[37] C. Amatore, C. Lefrou, F. Pflüger, *J. Electroanal. Chem.* **1989**, *270*, 43–59.

[38] a) F. Hartl, H. Luyten, H. A. Nieuwenhuis, G. C. Schoemaker, *Appl. Spectrosc.* **1994**, *48*, 1522–1528; b) T. Mahabiersing, H. Luyten, R. C. Nieuwendam, F. Hartl, *Collect. Czech. Chem. Commun.* **2003**, *68*, 1687–1709.

[39] Gaussian 03, Revision C.02, M. J. Frisch, G. W. Trucks, H. B. Schlegel, G. E. Scuseria, M. A. Robb, J. R. Cheeseman, J. A. Montgomery, Jr., T. Vreven, K. N. Kudin, J. C. Burant, J. M. Millam, S. S. Iyengar, J. Tomasi, V. Barone, B. Mennucci, M. Cossi, G. Scalmani, N. Rega, G. A. Petersson, H. Nakatsuji, M. Hada, M. Ehara, K. Toyota, R. Fukuda, J. Hasegawa, M. Ishida, T. Nakajima, Y. Honda, O. Kitao, H. Nakai, M. Klene, X. Li, J. E. Knox, H. P. Hratchian, J. B. Cross, V. Bakken, C. Adamo, J. Jaramillo, R. Gomperts, R. E. Stratmann, O. Yazyev, A. J. Austin, R. Cammi, C. Pomelli, J. W. Ochterski, P. Y. Ayala, K. Morokuma, G. A. Voth, P. Salvador, J. J. Dannenberg, V. G. Zakrzewski, S. Dapprich, A. D. Daniels, M. C. Strain, O. Farkas, D. K. Malick, A. D. Rabuck, K. Raghavachari, J. B. Foresman, J. V. Ortiz, Q. Cui, A. G. Baboul, S. Clifford, J. Cioslowski, B. B. Stefanov, G. Liu, A. Liashenko, P. Piskorz, I. Komaromi, R. L. Martin, D. J. Fox, T. Keith, M. A. Al-Laham, C. Y. Peng, A. Nanayakkara, M. Challacombe, P. M. W. Gill, B. Johnson, W. Chen, M. W. Wong, C. Gonzalez, J. A. Pople, Gaussian, Inc., Wallingford, CT, **2004**.

[40] a) A. D. Becke, *Phys. Rev. E* **1988**, *38*, 3098–3100; b) C. Lee, W. Yang, R. G. Parr, *Phys. Rev. B* **1988**, 37, 785–789.

[41] M. Bühl, W. Thiel, *Inorg. Chem.* **2004**, *43*, 6377–6382.

[42] a) P. C. Hariharan, J. A. Pople, *Theor. Chim. Acta* **1973**, *28*, 213–222; b) M. M. Francl, W. J. Petro, W. J. Hehre, J. S. Binkley, M. S. Gordon, D. J. DeFrees, J. A. Pople, *J. Chem. Phys.* **1982**, *77*, 3654–3665; c) M. Dolg, U. Wedig, H. Stoll, H. Preuss, *J. Chem. Phys.* **1987**, *86*, 866–872. Basis sets were obtained from the Extensible Computational Chemistry Environment Basis Set Database, Version 02/25/04, as developed and distributed by the Molecular Science Computing Facility, Environmental and Molecular Sciences Laboratory, which is part of the Pacific Northwest Laboratory, P.O. Box 999, Richland, Washington 99352, USA, and funded by the U.S. Department of Energy. The Pacific Northwest Laboratory is a multiprogram laboratory operated by Battelle Memorial Institute for the U.S. Department of Energy under contract DE-AC06-76RLO 1830.

[43] F. Wang, T. Ziegler, *Mol. Phys.* **2004**, *102*, 2585–2595.

Received: January 12, 2007
Revised: April 6, 2007
Published online: July 6, 2007

